Initial-state radiation measurement of the $e^+e^- \rightarrow \pi^+\pi^-\pi^+\pi^-$ cross section

J. P. Lees,[1] V. Poireau,[1] V. Tisserand,[1] J. Garra Tico,[2] E. Grauges,[2] M. Martinelli,[3a,3b] D. A. Milanes,[3a] A. Palano,[3a,3b] M. Pappagallo,[3a,3b] G. Eigen,[4] B. Stugu,[4] D. N. Brown,[5] L. T. Kerth,[5] Yu. G. Kolomensky,[5] G. Lynch,[5] H. Koch,[6] T. Schroeder,[6] D. J. Asgeirsson,[7] C. Hearty,[7] T. S. Mattison,[7] J. A. McKenna,[7] A. Khan,[8] V. E. Blinov,[9] A. R. Buzykaev,[9] V. P. Druzhinin,[9] V. B. Golubev,[9] E. A. Kravchenko,[9] A. P. Onuchin,[9] S. I. Serednyakov,[9] Yu. I. Skovpen,[9] E. P. Solodov,[9] K. Yu. Todyshev,[9] A. N. Yushkov,[9] M. Bondioli,[10] D. Kirkby,[10] A. J. Lankford,[10] M. Mandelkern,[10] D. P. Stoker,[10] H. Atmacan,[11] J. W. Gary,[11] F. Liu,[11] O. Long,[11] G. M. Vitug,[11] C. Campagnari,[12] T. M. Hong,[12] D. Kovalskyi,[12] J. D. Richman,[12] C. A. West,[12] A. M. Eisner,[13] J. Kroseberg,[13] W. S. Lockman,[13] A. J. Martinez,[13] T. Schalk,[13] B. A. Schumm,[13] A. Seiden,[13] C. H. Cheng,[14] D. A. Doll,[14] B. Echenard,[14] K. T. Flood,[14] D. G. Hitlin,[14] P. Ongmongkolkul,[14] F. C. Porter,[14] A. Y. Rakitin,[14] R. Andreassen,[15] M. S. Dubrovin,[15] Z. Huard,[15] B. T. Meadows,[15] M. D. Sokoloff,[15] L. Sun,[15] P. C. Bloom,[16] W. T. Ford,[16] A. Gaz,[16] M. Nagel,[16] U. Nauenberg,[16] J. G. Smith,[16] S. R. Wagner,[16] R. Ayad,[17,*] W. H. Toki,[17] B. Spaan,[18] M. J. Kobel,[19] K. R. Schubert,[19] R. Schwierz,[19] D. Bernard,[20] M. Verderi,[20] P. J. Clark,[21] S. Playfer,[21] D. Bettoni,[22a] C. Bozzi,[22a] R. Calabrese,[22a,22b] G. Cibinetto,[22a,22b] E. Fioravanti,[22a,22b] I. Garzia,[22a,22b] E. Luppi,[22a,22b] M. Munerato,[22a,22b] M. Negrini,[22a,22b] L. Piemontese,[22a] V. Santoro,[22a,22b] R. Baldini-Ferroli,[23] A. Calcaterra,[23] R. de Sangro,[23] G. Finocchiaro,[23] M. Nicolaci,[23] P. Patteri,[23] I. M. Peruzzi,[23,†] M. Piccolo,[23] M. Rama,[23] A. Zallo,[23] R. Contri,[24a,24b] E. Guido,[24a,24b] M. Lo Vetere,[24a,24b] M. R. Monge,[24a,24b] S. Passaggio,[24a] C. Patrignani,[24a,24b] E. Robutti,[24a] B. Bhuyan,[25] V. Prasad,[25] C. L. Lee,[26] M. Morii,[26] A. J. Edwards,[27] A. Adametz,[28] J. Marks,[28] U. Uwer,[28] F. U. Bernlochner,[29] M. Ebert,[29] H. M. Lacker,[29] T. Lueck,[29] P. D. Dauncey,[30] M. Tibbetts,[30] P. K. Behera,[31] U. Mallik,[31] C. Chen,[32] J. Cochran,[32] W. T. Meyer,[32] S. Prell,[32] E. I. Rosenberg,[32] A. E. Rubin,[32] A. V. Gritsan,[33] Z. J. Guo,[33] N. Arnaud,[34] M. Davier,[34] G. Grosdidier,[34] F. Le Diberder,[34] A. M. Lutz,[34] B. Malaescu,[34] P. Roudeau,[34] M. H. Schune,[34] A. Stocchi,[34] G. Wormser,[34] D. J. Lange,[35] D. M. Wright,[35] I. Bingham,[36] C. A. Chavez,[36] J. P. Coleman,[36] J. R. Fry,[36] E. Gabathuler,[36] D. E. Hutchcroft,[36] D. J. Payne,[36] C. Touramanis,[36] A. J. Bevan,[37] F. Di Lodovico,[37] R. Sacco,[37] M. Sigamani,[37] G. Cowan,[38] D. N. Brown,[39] C. L. Davis,[39] A. G. Denig,[40] M. Fritsch,[40] W. Gradl,[40] A. Hafner,[40] E. Prencipe,[40] K. E. Alwyn,[41] D. Bailey,[41] R. J. Barlow,[41,‡] G. Jackson,[41] G. D. Lafferty,[41] E. Behn,[42] R. Cenci,[42] B. Hamilton,[42] A. Jawahery,[42] D. A. Roberts,[42] G. Simi,[42] C. Dallapiccola,[43] R. Cowan,[44] D. Dujmic,[44] G. Sciolla,[44] D. Lindemann,[45] P. M. Patel,[45] S. H. Robertson,[45] M. Schram,[45] P. Biassoni,[46a,46b] A. Lazzaro,[46a,46b] V. Lombardo,[46a] N. Neri,[46a,46b] F. Palombo,[46a,46b] S. Stracka,[46a,46b] L. Cremaldi,[47] R. Godang,[47,§] R. Kroeger,[47] P. Sonnek,[47] D. J. Summers,[47] X. Nguyen,[48] P. Taras,[48] G. De Nardo,[49a,49b] D. Monorchio,[49a,49b] G. Onorato,[49a,49b] C. Sciacca,[49a,49b] G. Raven,[50] H. L. Snoek,[50] C. P. Jessop,[51] K. J. Knoepfel,[51] J. M. LoSecco,[51] W. F. Wang,[51] K. Honscheid,[52] R. Kass,[52] J. Brau,[53] R. Frey,[53] N. B. Sinev,[53] D. Strom,[53] E. Torrence,[53] E. Feltresi,[54a,54b] N. Gagliardi,[54a,54b] M. Margoni,[54a,54b] M. Morandin,[54a] M. Posocco,[54a] M. Rotondo,[54a] F. Simonetto,[54a,54b] R. Stroili,[54a,54b] S. Akar,[55] E. Ben-Haim,[55] M. Bomben,[55] G. R. Bonneaud,[55] H. Briand,[55] G. Calderini,[55] J. Chauveau,[55] O. Hamon,[55] Ph. Leruste,[55] G. Marchiori,[55] J. Ocariz,[55] S. Sitt,[55] M. Biasini,[56a,56b] E. Manoni,[56a,56b] S. Pacetti,[56a,56b] A. Rossi,[56a,56b] C. Angelini,[57a,57b] G. Batignani,[57a,57b] S. Bettarini,[57a,57b] M. Carpinelli,[57a,57b,‖] G. Casarosa,[57a,57b] A. Cervelli,[57a,57b] F. Forti,[57a,57b] M. A. Giorgi,[57a,57b] A. Lusiani,[57a,57c] B. Oberhof,[57a,57b] E. Paoloni,[57a,57b] A. Perez,[57a] G. Rizzo,[57a,57b] J. J. Walsh,[57a] D. Lopes Pegna,[58] C. Lu,[58] J. Olsen,[58] A. J. S. Smith,[58] A. V. Telnov,[58] F. Anulli,[59a] G. Cavoto,[59a] R. Faccini,[59a,59b] F. Ferrarotto,[59a] F. Ferroni,[59a,59b] M. Gaspero,[59a,59b] L. Li Gioi,[59a] M. A. Mazzoni,[59a] G. Piredda,[59a] C. Bünger,[60] O. Grünberg,[60] T. Hartmann,[60] T. Leddig,[60] H. Schröder,[60] R. Waldi,[60] T. Adye,[61] E. O. Olaiya,[61] F. F. Wilson,[61] S. Emery,[62] G. Hamel de Monchenault,[62] G. Vasseur,[62] Ch. Yèche,[62] D. Aston,[63] D. J. Bard,[63] R. Bartoldus,[63] C. Cartaro,[63] M. R. Convery,[63] J. Dorfan,[63] G. P. Dubois-Felsmann,[63] W. Dunwoodie,[63] R. C. Field,[63] M. Franco Sevilla,[63] B. G. Fulsom,[63] A. M. Gabareen,[63] M. T. Graham,[63] P. Grenier,[63] C. Hast,[63] W. R. Innes,[63] M. H. Kelsey,[63] H. Kim,[63] P. Kim,[63] M. L. Kocian,[63] D. W. G. S. Leith,[63] P. Lewis,[63] S. Li,[63] B. Lindquist,[63] S. Luitz,[63] V. Luth,[63] H. L. Lynch,[63] D. B. MacFarlane,[63] D. R. Muller,[63] H. Neal,[63] S. Nelson,[63] I. Ofte,[63] M. Perl,[63] T. Pulliam,[63] B. N. Ratcliff,[63] A. Roodman,[63] A. A. Salnikov,[63] R. H. Schindler,[63] A. Snyder,[63] D. Su,[63] M. K. Sullivan,[63] J. Va'vra,[63] A. P. Wagner,[63] M. Weaver,[63] W. J. Wisniewski,[63] M. Wittgen,[63] D. H. Wright,[63] H. W. Wulsin,[63] A. K. Yarritu,[63] C. C. Young,[63] V. Ziegler,[63] W. Park,[64] M. V. Purohit,[64] R. M. White,[64] J. R. Wilson,[64] A. Randle-Conde,[65] S. J. Sekula,[65] M. Bellis,[66] J. F. Benitez,[66] P. R. Burchat,[66] T. S. Miyashita,[66] M. S. Alam,[67] J. A. Ernst,[67] R. Gorodeisky,[68] N. Guttman,[68] D. R. Peimer,[68] A. Soffer,[68] P. Lund,[69] S. M. Spanier,[69] R. Eckmann,[70] J. L. Ritchie,[70] A. M. Ruland,[70] C. J. Schilling,[70] R. F. Schwitters,[70] B. C. Wray,[70] J. M. Izen,[71] X. C. Lou,[71] F. Bianchi,[72a,72b] D. Gamba,[72a,72b] L. Lanceri,[73a,73b] L. Vitale,[73a,73b] F. Martinez-Vidal,[74]

A. Oyanguren,[74] H. Ahmed,[75] J. Albert,[75] Sw. Banerjee,[75] H. H. F. Choi,[75] G. J. King,[75] R. Kowalewski,[75]
M. J. Lewczuk,[75] I. M. Nugent,[75] J. M. Roney,[75] R. J. Sobie,[75] N. Tasneem,[75] T. J. Gershon,[76] P. F. Harrison,[76]
T. E. Latham,[76] E. M. T. Puccio,[76] H. R. Band,[77] S. Dasu,[77] Y. Pan,[77] R. Prepost,[77] and S. L. Wu[77]

(*BABAR* Collaboration)

[1]*Laboratoire d'Annecy-le-Vieux de Physique des Particules (LAPP), Université de Savoie,
CNRS/IN2P3, F-74941 Annecy-Le-Vieux, France*
[2]*Universitat de Barcelona, Facultat de Fisica, Departament ECM, E-08028 Barcelona, Spain*
[3a]*INFN Sezione di Bari, I-70126 Bari, Italy*
[3b]*Dipartimento di Fisica, Università di Bari, I-70126 Bari, Italy*
[4]*University of Bergen, Institute of Physics, N-5007 Bergen, Norway*
[5]*Lawrence Berkeley National Laboratory and University of California, Berkeley, California 94720, USA*
[6]*Ruhr Universität Bochum, Institut für Experimentalphysik 1, D-44780 Bochum, Germany*
[7]*University of British Columbia, Vancouver, British Columbia, Canada V6T 1Z1*
[8]*Brunel University, Uxbridge, Middlesex UB8 3PH, United Kingdom*
[9]*Budker Institute of Nuclear Physics, Novosibirsk 630090, Russia*
[10]*University of California at Irvine, Irvine, California 92697, USA*
[11]*University of California at Riverside, Riverside, California 92521, USA*
[12]*University of California at Santa Barbara, Santa Barbara, California 93106, USA*
[13]*University of California at Santa Cruz, Institute for Particle Physics, Santa Cruz, California 95064, USA*
[14]*California Institute of Technology, Pasadena, California 91125, USA*
[15]*University of Cincinnati, Cincinnati, Ohio 45221, USA*
[16]*University of Colorado, Boulder, Colorado 80309, USA*
[17]*Colorado State University, Fort Collins, Colorado 80523, USA*
[18]*Technische Universität Dortmund, Fakultät Physik, D-44221 Dortmund, Germany*
[19]*Technische Universität Dresden, Institut für Kern- und Teilchenphysik, D-01062 Dresden, Germany*
[20]*Laboratoire Leprince-Ringuet, Ecole Polytechnique, CNRS/IN2P3, F-91128 Palaiseau, France*
[21]*University of Edinburgh, Edinburgh EH9 3JZ, United Kingdom*
[22a]*INFN Sezione di Ferrara, I-44100 Ferrara, Italy*
[22b]*Dipartimento di Fisica, Università di Ferrara, I-44100 Ferrara, Italy*
[23]*INFN Laboratori Nazionali di Frascati, I-00044 Frascati, Italy*
[24a]*INFN Sezione di Genova, I-16146 Genova, Italy*
[24b]*Dipartimento di Fisica, Università di Genova, I-16146 Genova, Italy*
[25]*Indian Institute of Technology Guwahati, Guwahati, Assam, 781 039, India*
[26]*Harvard University, Cambridge, Massachusetts 02138, USA*
[27]*Harvey Mudd College, Claremont, California 91711, USA*
[28]*Universität Heidelberg, Physikalisches Institut, Philosophenweg 12, D-69120 Heidelberg, Germany*
[29]*Humboldt-Universität zu Berlin, Institut für Physik, Newtonstr. 15, D-12489 Berlin, Germany*
[30]*Imperial College London, London, SW7 2AZ, United Kingdom*
[31]*University of Iowa, Iowa City, Iowa 52242, USA*
[32]*Iowa State University, Ames, Iowa 50011-3160, USA*
[33]*Johns Hopkins University, Baltimore, Maryland 21218, USA*
[34]*Laboratoire de l'Accélérateur Linéaire, IN2P3/CNRS et Université Paris-Sud 11,
Centre Scientifique d'Orsay, B. P. 34, F-91898 Orsay Cedex, France*
[35]*Lawrence Livermore National Laboratory, Livermore, California 94550, USA*
[36]*University of Liverpool, Liverpool L69 7ZE, United Kingdom*
[37]*Queen Mary, University of London, London, E1 4NS, United Kingdom*
[38]*University of London, Royal Holloway and Bedford New College, Egham, Surrey TW20 0EX, United Kingdom*
[39]*University of Louisville, Louisville, Kentucky 40292, USA*
[40]*Johannes Gutenberg-Universität Mainz, Institut für Kernphysik, D-55099 Mainz, Germany*
[41]*University of Manchester, Manchester M13 9PL, United Kingdom*
[42]*University of Maryland, College Park, Maryland 20742, USA*
[43]*University of Massachusetts, Amherst, Massachusetts 01003, USA*
[44]*Massachusetts Institute of Technology, Laboratory for Nuclear Science,
Cambridge, Massachusetts 02139, USA*
[45]*McGill University, Montréal, Québec, Canada H3A 2T8*
[46a]*INFN Sezione di Milano, I-20133 Milano, Italy*
[46b]*Dipartimento di Fisica, Università di Milano, I-20133 Milano, Italy*

[47]University of Mississippi, University, Mississippi 38677, USA

[48]Université de Montréal, Physique des Particules, Montréal, Québec, Canada H3C 3J7

[49a]INFN Sezione di Napoli, I-80126 Napoli, Italy

[49b]Dipartimento di Scienze Fisiche, Università di Napoli Federico II, I-80126 Napoli, Italy

[50]NIKHEF, National Institute for Nuclear Physics and High Energy Physics, NL-1009 DB Amsterdam, The Netherlands

[51]University of Notre Dame, Notre Dame, Indiana 46556, USA

[52]Ohio State University, Columbus, Ohio 43210, USA

[53]University of Oregon, Eugene, Oregon 97403, USA

[54a]INFN Sezione di Padova, I-35131 Padova, Italy

[54b]Dipartimento di Fisica, Università di Padova, I-35131 Padova, Italy

[55]Laboratoire de Physique Nucléaire et de Hautes Energies, IN2P3/CNRS, Université Pierre et Marie Curie-Paris6, Université Denis Diderot-Paris7, F-75252 Paris, France

[56a]INFN Sezione di Perugia, I-06100 Perugia, Italy

[56b]Dipartimento di Fisica, Università di Perugia, I-06100 Perugia, Italy

[57a]INFN Sezione di Pisa, I-56127 Pisa, Italy

[57b]Dipartimento di Fisica, Università di Pisa, I-56127 Pisa, Italy

[57c]Scuola Normale Superiore di Pisa, I-56127 Pisa, Italy

[58]Princeton University, Princeton, New Jersey 08544, USA

[59a]INFN Sezione di Roma, I-00185 Roma, Italy

[59b]Dipartimento di Fisica, Università di Roma La Sapienza, I-00185 Roma, Italy

[60]Universität Rostock, D-18051 Rostock, Germany

[61]Rutherford Appleton Laboratory, Chilton, Didcot, Oxon, OX11 0QX, United Kingdom

[62]CEA, Irfu, SPP, Centre de Saclay, F-91191 Gif-sur-Yvette, France

[63]SLAC National Accelerator Laboratory, Stanford, California 94309, USA

[64]University of South Carolina, Columbia, South Carolina 29208, USA

[65]Southern Methodist University, Dallas, Texas 75275, USA

[66]Stanford University, Stanford, California 94305-4060, USA

[67]State University of New York, Albany, New York 12222, USA

[68]Tel Aviv University, School of Physics and Astronomy, Tel Aviv, 69978, Israel

[69]University of Tennessee, Knoxville, Tennessee 37996, USA

[70]University of Texas at Austin, Austin, Texas 78712, USA

[71]University of Texas at Dallas, Richardson, Texas 75083, USA

[72a]INFN Sezione di Torino, I-10125 Torino, Italy

[72b]Dipartimento di Fisica Sperimentale, Università di Torino, I-10125 Torino, Italy

[73a]INFN Sezione di Trieste, I-34127 Trieste, Italy

[73b]Dipartimento di Fisica, Università di Trieste, I-34127 Trieste, Italy

[74]IFIC, Universitat de Valencia-CSIC, E-46071 Valencia, Spain

[75]University of Victoria, Victoria, British Columbia, Canada V8W 3P6

[76]Department of Physics, University of Warwick, Coventry CV4 7AL, United Kingdom

[77]University of Wisconsin, Madison, Wisconsin 53706, USA

We study the process $e^+e^- \rightarrow \pi^+\pi^-\pi^+\pi^-\gamma$, with a photon emitted from the initial-state electron or positron, using 454.3 fb^{-1} of data collected with the *BABAR* detector at SLAC, corresponding to approximately $260\,000$ signal events. We use these data to extract the nonradiative $\sigma(e^+e^- \rightarrow \pi^+\pi^-\pi^+\pi^-)$ cross section in the energy range from 0.6 to 4.5 GeV. The total uncertainty of the cross section measurement in the peak region is less than 3%, higher in precision than the corresponding results obtained from energy scan data.

---

[*]Now at Temple University, Philadelphia, Pennsylvania 19122, USA.

[†]Also with Università di Perugia, Dipartimento di Fisica, Perugia, Italy.

[‡]Now at the University of Huddersfield, Huddersfield HD1 3DH, United Kingdom.

[§]Now at University of South Alabama, Mobile, Alabama 36688, USA.

[‖]Also with Università di Sassari, Sassari, Italy.

I. INTRODUCTION

While the electroweak contribution to the anomalous magnetic moment of the muon $a_\mu = \frac{1}{2}(g_\mu - 2)$ can be calculated with sub-ppm precision, the hadronic contribution a_μ^{had} cannot be evaluated by means of perturbative techniques within quantum chromodynamics (QCD). However, it is possible to relate a_μ^{had} via a dispersion relation to hadronic cross section $\sigma(e^+ e^- \rightarrow \text{hadrons})$ data [1]. Thus, hadronic cross section measurements are important for the standard model prediction of a_μ, which differs by more than three standard deviations from a recent direct Brookhaven National Laboratory measurement [2].

The study of initial-state radiation (ISR) events at an $e^+ e^-$ collider with a fixed center-of-mass (CM) energy E_{CM} allows high-precision measurements of the cross section of exclusive hadronic channels for energies below the nominal E_{CM} and is complementary to studies based on an energy scan. Use of the ISR technique is discussed in Refs. [3–6]. Previously, we used this technique to investigate low-multiplicity hadronic processes at effective CM energies below 5 GeV [7–15].

The ISR cross section $\sigma_{f,\gamma}$ for a specific final-state f depends on the nonradiative cross section σ_f and is given by [5]

$$\frac{d\sigma_{f,\gamma}(s, M_{\text{had}})}{dM_{\text{had}}} = \frac{2M_{\text{had}}}{s} \cdot W(s, x, C^*) \cdot \sigma_f(M_{\text{had}}), \quad (1)$$

where $x = 2 \cdot E_\gamma^* / \sqrt{s}$, $\sqrt{s}$ is the nominal CM energy, E_γ^* is the energy of the ISR photon,[1] and $M_{\text{had}} = \sqrt{s(1-x)}$. The radiator function $W(s, x, C^*)$, which describes the probability for the emission of an ISR photon in the polar angle range $|\cos\theta_\gamma^*| < C^*$, is determined to next-to-leading order (NLO) ISR with the PHOKHARA software package [16]. θ^* is the angle of the emitted γ with respect to the direction of the incoming e^-. Effects of final-state radiation (FSR), which are neglected in Eq. (1), are studied and corrected for as explained in Sec. VI.

Recently, cross section measurements with approximately 1% precision have been presented for the $\pi^+ \pi^-$ final state [15,17,18]. These measurements have led to a significant reduction in the uncertainty of a_μ^{had} [19]. As a consequence, a large relative contribution to the uncertainty of a_μ^{had} now arises from the energy range 1 GeV $< E < 2$ GeV [20]. In this energy range, the hadronic cross section is dominated by the exclusive $e^+ e^- \rightarrow \pi^+ \pi^- \pi^+ \pi^-$ and $\pi^+ \pi^- \pi^0 \pi^0$ channels.

This paper reports results from an ISR analysis of the $e^+ e^- \rightarrow \pi^+ \pi^- \pi^+ \pi^- \gamma$ process. The four-pion mass $M_{4\pi}$ serves as the effective hadronic E_{CM} value. It is an update of our earlier study [8], based on a data sample

---

[1] * refers to the nominal CM frame.

that is five times larger. We perform a more detailed study of systematic effects and thereby obtain significant improvements in both the statistical and systematic uncertainties.

The outline of this paper is as follows. Section II describes the *BABAR* detector and the data set used in this analysis. The primary event selection is presented in Sec. III. After discussing the background suppression (Sec. IV) and the acceptance and efficiency studies (Sec. V), the extraction of the nonradiative cross section is described in Sec. VI. A qualitative analysis of the intermediate subsystems and a quantitative measurement of the J/ψ and $\psi(2S)$ branching fractions follows in Sec. VII. A summary is given in Sec. VIII.

II. THE *BABAR* DETECTOR AND DATA SET

The data used in this analysis were collected with the *BABAR* detector at the PEP-II asymmetric energy $e^+ e^-$ storage rings at the SLAC National Accelerator Laboratory. A total integrated luminosity of 454.3 fb^{-1} is used, comprised of 413.1 fb^{-1} collected at the $\Upsilon(4S)$ resonance peak, and 41.2 fb^{-1} collected 40 MeV below the peak.

The *BABAR* detector is described in detail elsewhere [21]. The reconstruction of charged-particle tracks is performed with the tracking system, which is comprised of a five-layer silicon vertex tracker and a 40-layer drift chamber, both in a 1.5 T axial magnetic field. Separation of electrons, protons, charged pions, and charged kaons is achieved using Cherenkov angles measured with the detector of internally reflected Cherenkov light in combination with specific ionization dE/dx measurements from the silicon vertex tracker and drift chamber. The CsI(Tl) electromagnetic calorimeter (EMC) measures the energy of photons and electrons. Muon identification is provided by the instrumented flux return.

A simulation package developed for radiative processes, AFKQED, is used to determine detector acceptance and reconstruction efficiencies. Hadronic final states, including $\pi^+ \pi^- \pi^+ \pi^- \gamma$, are simulated based on an approach of Czyż and Kühn [22]. The underlying model assumes dominance of the $a_1(1260)\pi$ final-state as was reported in Refs. [23,24]. Because of the dominant decay $a_1(1260) \rightarrow \rho^0 \pi$, each event contains one pair of pions from ρ^0 decay. The simulation of multiple soft-photon emission from the initial state is performed via a structure function technique [25,26]. Extra radiation from the final state particles is simulated by the PHOTOS package [27]. The accuracy of the radiative corrections is about 1%. A new version of PHOKHARA [16], which incorporates the results of recent studies [8] on intermediate resonances, is used to investigate the influence of these intermediate resonances on the acceptance.

The simulated events are subjected to simulation of the detector [28] and the same analysis procedures as the data.

Variations in detector and background conditions over the course of the experiment are modeled.

A large number of potential background processes are simulated, including the ISR processes $K^+K^-\pi^+\pi^-\gamma$ and $K_S^0 K^\pm \pi^\mp \gamma$. Other ISR background channels are also examined. Either the remaining number of events after the event selection is negligible in comparison to other uncertainties, or dedicated methods for background rejection are implemented as described in Sec. IV. Non-ISR backgrounds resulting from $e^+e^- \rightarrow q\bar{q}$ ($q = u, d, s, c$) continuum events are modeled using the JETSET generator [29], while those from $e^+e^- \rightarrow \tau^+\tau^-$ are modeled with KORALB [30]. The cross sections of the ISR channels and the branching fractions of the inclusive processes leading to final states similar to our signal are known with about 10% accuracy or better, which is sufficient for the purpose of this measurement. The contribution from $\Upsilon(4S) \rightarrow \pi^+\pi^-\pi^+\pi^-\gamma$ events is negligible.

III. PRIMARY EVENT SELECTION AND KINEMATIC FIT

Charged tracks are selected by requiring that they originate from the collision region (transverse distance of closest approach to the nominal interaction point $d_T < 1.5$ cm, and in the beam direction $d_Z < 2.5$ cm), and that they have a polar angle θ_{ch} in the well-understood acceptance region of the detector (0.5 rad $< \theta_{\text{ch}} < 2.4$ rad). The coordinate system has the z-axis in the direction of the incoming e^- beam. Tracks with transverse momenta less than 100 MeV/c or that are consistent with being an electron are rejected. Photon candidates are required to have a minimum energy $E_{\gamma,\text{CM}} > 50$ MeV. The ISR photon candidate is restricted to the polar angle range inside the well-understood acceptance region of the EMC (0.35 rad $< \theta_\gamma < 2.4$ rad) and a minimum energy of $E_{\text{ISR}} > 3$ GeV is required.

Radiative Bhabha events are suppressed by requiring the two most energetic tracks of the event not to be identified as electrons. The minimum angle between a charged track and the ISR photon $\Delta\psi$ is required to satisfy $\Delta\psi > 1.0$ rad, in order to select the back-to-back topology between the charged tracks and photon typical for ISR events.

A kinematic fit procedure with four constraints (4C) is applied to events with four tracks satisfying these criteria. The constrained fit uses the measured momenta and directions of the charged particles and the ISR photon and the corresponding error matrix to solve the energy-momentum equation. To provide accurate photon parameters to the kinematic fit, a precise alignment and an energy calibration of the EMC are performed using a $\mu^+\mu^-\gamma$ sample. This improves the data-simulation agreement in the goodness-of-fit distributions (see below) of the kinematic fit. The $\mu^+\mu^-\gamma$ sample is also used to identify and measure differences between the data and the simulation (MC) in the photon detection efficiency.

The kinematic fit is performed assuming the $\pi^+\pi^-\pi^+\pi^-\gamma$ signal hypothesis. If two tracks are identified as kaons the fit is also performed under the $K^+K^-\pi^+\pi^-\gamma$ hypothesis. The fitting routine returns a goodness-of-fit quantity $\chi^2_{4\pi}$ and $\chi^2_{2K2\pi}$, respectively, which we use to select signal events and to suppress $K^+K^-\pi^+\pi^-\gamma$ background.

Figures 1(a) and 1(b) show the measured $\chi^2_{4\pi}$ distribution before background subtraction in comparison to the distribution from the simulated signal sample. The results are shown on logarithmic and linear scales. The distributions are normalized to the number of events with $\chi^2_{4\pi} < 10$. Figure 1(c) shows the $\chi^2_{4\pi}$ distribution for the main backgrounds. The difference between measured and simulated samples is shown in Fig. 1(d) for $\chi^2_{4\pi} > 10$. For large values of $\chi^2_{4\pi}$, the difference is approximately flat, and is consistent with the sum of backgrounds shown in Fig. 1(c). At small $\chi^2_{4\pi}$ values, resolution effects cause the difference to decrease. This is studied with a clean sample of four pions and one photon where the resolution effect is visible for $\chi^2_{4\pi} < 20$. To avoid a bias due to the resolution difference between the data and simulation, the requirement $\chi^2_{4\pi} < 30$ is used in the event analysis. In addition, background channels are suppressed using dedicated
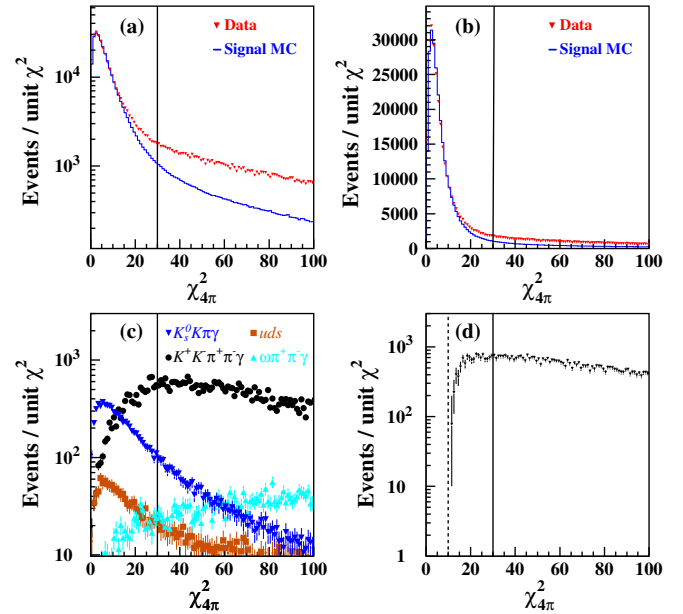
FIG. 1 (color online). (a,b) The $\chi^2_{4\pi}$ distribution for data without background subtraction (triangles) and signal MC (histogram) on a logarithmic and linear scale. (c) MC distributions of the principal backgrounds. (d) The difference between the measured and the simulated distributions from part (a,b). The dashed and solid vertical lines indicate the boundaries with the $0 < \chi^2_{4\pi} < 10$ region used for normalization and the $\chi^2_{4\pi} < 30$ requirement, respectively.

vetoes and particle identification (PID) selectors, as discussed in Sec. IV.

IV. BACKGROUND REJECTION

Because of large variations in the signal-to-background ratio across different 4π mass $M_{4\pi}$ regions, different strategies are implemented to eliminate background, depending on the $M_{4\pi}$ region. Figure 2(a) shows the $M_{4\pi}$ distribution under the $\pi^+\pi^-\pi^+\pi^-\gamma$ hypothesis with the requirement $\chi^2_{4\pi} < 30$. The results are shown for the data and for the sum of the simulated ISR channels $e^+e^- \to K^+K^-\pi^+\pi^-\gamma$, $e^+e^- \to K^0_S K^\pm \pi^\mp \gamma$, $e^+e^- \to \omega\pi^+\pi^-\gamma$ and the non-ISR continuum background. In Fig. 2(b), these background contributions are shown individually. The $\chi^2_{4\pi}$ requirement effectively eliminates the $\omega\pi^+\pi^-\gamma$ background: according to simulation, only 450 $\omega\pi^+\pi^-\gamma$ events remain after applying this restriction, in comparison to 260 000 signal events with a very similar $M_{4\pi}$ distribution, leading to a relative contribution of less than $\approx 0.2\%$. At very low invariant masses, $M_{4\pi} < 1.1$ GeV/c^2, the background contributions from $\pi^+\pi^-\gamma\gamma$ and $\pi^+\pi^-\pi^0\gamma$ are large and not included in Fig. 2. In this threshold region, the signal-to-background ratio is approximately 1:5. In the peak region, 1.1 GeV/$c^2 < M_{4\pi} < 2.2$ GeV/c^2, the background contamination is at the level of 3–4%, dominated by $e^+e^- \to K^+K^-\pi^+\pi^-\gamma$ and $e^+e^- \to K^0_S K^\pm \pi^\mp \gamma$. At high $M_{4\pi}$, the background level rises to about 10%, mainly due to the additional contribution of *uds*-continuum events.

A clear peak from $J/\psi \to \pi^+\pi^-\pi^+\pi^-$ is visible in the distributions of Fig. 2. In addition, the data exhibit a narrow peak in the $\psi(2S)$ mass region, due to the decay $\psi(2S) \to \pi^+\pi^- J/\psi$ with $J/\psi \to \mu^+\mu^-$ and misidentified muons. The rejection of this background is described in subsection IV B.
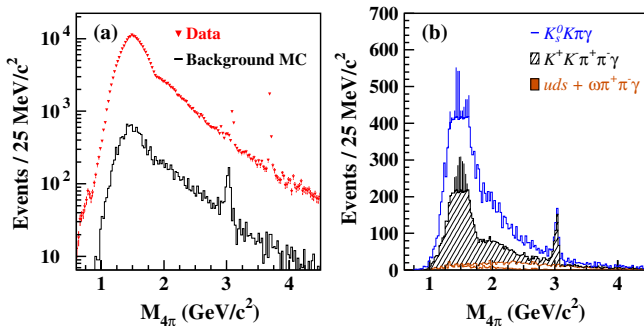

FIG. 2 (color online). (a) The $\pi^+\pi^-\pi^+\pi^-$ invariant mass distribution of $\pi^+\pi^-\pi^+\pi^-\gamma$ ISR events (triangles) for the main selection and the sum of simulated $K^+K^-\pi^+\pi^-\gamma$, $K^0_S K^\pm \pi^\mp \gamma$, $\omega\pi^+\pi^-\gamma$ and nonradiative *uds*-continuum background (histogram). The large $\pi^+\pi^-\gamma\gamma$ and $\pi^+\pi^-\pi^0\gamma$ background contribution in the threshold region ($M_{4\pi} < 1.1$ GeV/c^2) is not included in the simulation. (b) The individual simulated background channel contributions from top to bottom as indicated in the legend.

A. Background in the peak region
(1.1 GeV/$c^2 < M_{4\pi} < 2.2$ GeV/c^2)

The dominant background in the peak region is from the ISR processes $e^+e^- \to K^+K^-\pi^+\pi^-\gamma$ and $e^+e^- \to K^0_S K^\pm \pi^\mp \gamma$. We utilize two different approaches to evaluate the background and use the difference between the methods to estimate the systematic uncertainty related to the background subtraction. The background subtraction itself is performed using method 2.

1. Method 1: Subtract simulated background

For background subtraction via method 1, we use recent measurements of the most important background channels, $K^+K^-\pi^+\pi^-\gamma$ [13] and $K^0_S K^\pm \pi^\mp \gamma$ [14]. We tune AFKQED according to these measurements and use the resulting predictions to evaluate the contributions of these channels to the $M_{4\pi}$ spectrum.

2. Method 2: Background suppression

This method is a hybrid approach. We impose specific requirements in order to suppress the $K^+K^-\pi^+\pi^-\gamma$ and $K^0_S K^\pm \pi^\mp \gamma$ backgrounds: the so-called $K^+K^-\pi^+\pi^-\gamma$ and $K^0_S K^\pm \pi^\mp \gamma$ vetoes. The remaining background is then subtracted according to method 1.

$K^0_S K^\pm \pi^\mp \gamma$ events are vetoed if one of the tracks is identified as a $K^\pm$. The identification algorithm has an efficiency of 80–90% per track and a π misidentification probability of 0.25%. In addition, we require the invariant mass formed from two of the three remaining tracks to lie within 35 MeV/c^2 of the nominal K^0_S mass [31]. According to simulation, this method removes 74% of the $K^0_S K^\pm \pi^\mp \gamma$ background but only 1% of signal.

$K^+K^-\pi^+\pi^-\gamma$ events are rejected if two oppositely-charged tracks are identified as kaons and the requirement $\chi^2_{2K2\pi} < 10$ is fulfilled. The $K^\pm$ identification algorithm has an identification efficiency of 85–95% per track and a π misidentification probability of 1%. This requirement removes less than 0.1% of the signal, but 55% of the $K^+K^-\pi^+\pi^-\gamma$ background.

Comparing the results of the two methods yields a systematic uncertainty of 1.0% on the $e^+e^- \to \pi^+\pi^-\pi^+\pi^-$ cross section in the peak region.

B. Background at large invariant masses
($M_{4\pi} > 2.2$ GeV/c^2)

From Fig. 2(b) it is seen that the *uds* continuum background is significant in the $M_{4\pi} > 2.2$ GeV/c^2 mass region. The largest contribution is from $e^+e^- \to \pi^+\pi^-\pi^+\pi^-\pi^0$ events in which one of the photons from the $\pi^0 \to \gamma\gamma$ decay is mistaken for the γ_{ISR}. The similar kinematic configuration of the *uds*-continuum events causes a peak at small values of $\chi^2_{4\pi}$. We estimate this background by measuring the π^0 yield from a fit to the π^0 mass peak in the two-photon invariant mass distribution of

the ISR photon candidate with any other photon candidate. We then scale the MC π^0 rate to give the same yield as observed in the data. The corresponding scaling factor is extracted with a relative uncertainty of about 22%. The normalized *uds*-continuum MC sample is used for background subtraction. The corresponding systematic uncertainty on the cross section measurement is 0.5% in the peak region and rises up to 1.5% for $M_{4\pi} >$ 2.8 GeV/c^2.

There is an additional peaking background contribution in the charmonium region. Figure 3(a) shows the invariant mass distribution under the $\pi^+\pi^-\pi^+\pi^-$ hypothesis for the data. Peaks corresponding to the J/ψ and $\psi(2S)$ resonances are clearly seen. In Fig. 3(b), the invariant $\pi^+\pi^-$ mass $M_{2\pi}$ distribution for events within the $\psi(2S)$ (3.65 GeV/$c^2 < M_{4\pi} <$ 3.75 GeV/c^2) mass region are plotted. The distribution contains four entries per event. The J/ψ peak is clearly visible. The $J/\psi \to \pi^+\pi^-$ branching fraction is about a factor 400 smaller than that of $J/\psi \to \mu^+\mu^-$ [31]. No PID selector is used in the sample selection. In addition, the kinematic fit does not suppress $\pi^+\pi^-\mu^+\mu^-$ events, because the mass difference between muons and pions is only 34 MeV/c^2, which is negligible due to the fact that they are highly relativistic, being emitted from the J/ψ. Thus, the observed peak is likely dominated by $\psi(2S) \to \pi^+\pi^-\mu^+\mu^-$ decays. To remove this background, we reject events that have $M_{4\pi}$
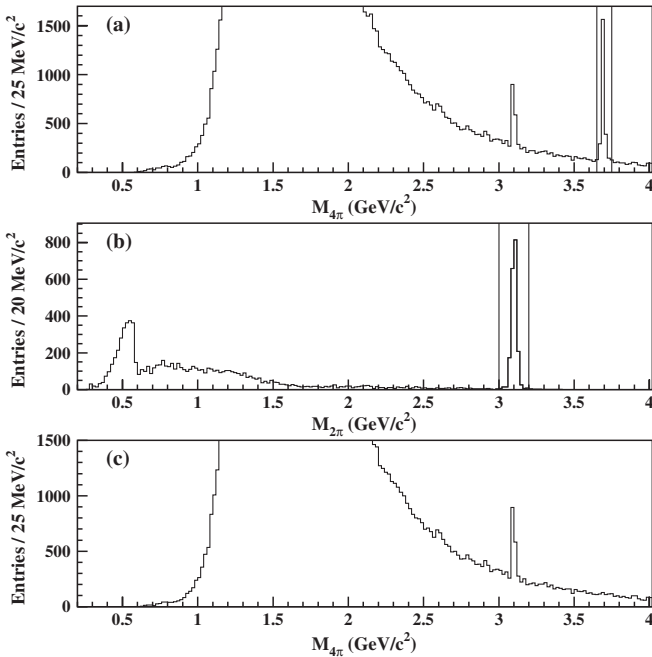

FIG. 3. (a) Invariant mass distribution under the $\pi^+\pi^-\pi^+\pi^-$ hypothesis for the data; (b) $\pi^+\pi^-$ invariant mass distribution for events with $M_{4\pi}$ in the $\psi(2S)$ mass region represented by the vertical lines in (a) (4 entries per event); (c) Same as part (a) after removing entries of the invariant $\pi^+\pi^-$-mass in the J/ψ mass region represented by the vertical lines in (b).

in the $\psi(2S)$ region and an $M_{2\pi}$ value consistent with the J/ψ. The corresponding $M_{4\pi}$ distribution after the $\psi(2S)$ veto is shown in Fig. 3(c).

C. Background at small invariant masses ($M_{4\pi} <$ 1.1 GeV/c^2)

Background in the threshold region, i.e., below 1.1 GeV/c^2, is dominated by two processes: γ conversion of a real photon in the detector material, and conversion of a virtual photon at the primary interaction vertex (Dalitz conversion). In $e^+e^- \to \pi^+\pi^-\pi^0\gamma_{ISR}$ events, one of the photons from the π^0 decay can convert the detector material into an e^+e^- pair, and both the e^+ and the e^- can be misidentified as pions. Moreover, $e^+e^- \to \pi^+\pi^-\gamma_{ISR}\gamma$ events in which the non-ISR photon converts into an e^+e^- pair contribute a similar background. The second source of background in this mass region is $e^+e^- \to \pi^+\pi^-\gamma_{ISR}e^+e^-$ events in which the e^+e^- pair arises from a Dalitz conversion process. Two methods are used to remove these background channels.

1. Method 1: Vetoes for Dalitz conversion and conversion in the detector

The first method vetoes events with either a primary vertex probability less than 10^{-8} or with two identified electrons. Electrons are identified using an algorithm with an efficiency of 99% and a pion misidentification rate of 5–10% depending on the transverse momentum of the track. The first requirement is not sufficient to reject background events with highly-energetic electrons or positrons, which have a vertex probability similar to nonconversion events. MC study shows that the combination of both requirements yields a background rejection larger than 99% while removing less than 6% of signal.

2. Method 2: Pion identification

The second method requires all four tracks to be identified as pions, using a selector with an efficiency of 97–99% and an electron misidentification probability of 5–7% depending on the transverse momentum of the track. There is, however, a difference in efficiency between the data and MC simulation of approximately 0.5–1% per track (2–4% shift per event). Therefore, this selector is not used in the peak region, where the background contribution is very low.

Both methods remove a large fraction of the conversions and yield results that are consistent with each other. We present our primary results using the pion selection method, as the systematic uncertainties on its inputs are better understood. Comparing the cross section results using the two methods leads to a systematic uncertainty estimate of 3%. It should be noted that the $\rho(770)^0$ peak is strongly suppressed, but is still visible as a shoulder after background subtraction, as shown in Fig. 4.
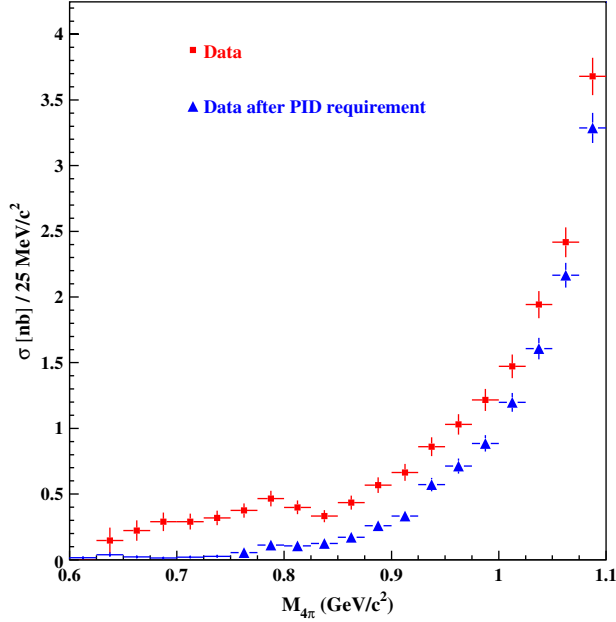
FIG. 4 (color online). $\pi^+\pi^-\pi^+\pi^-\gamma$ cross section in the threshold region for the data (squares) and for the data after requiring each track to satisfy a dedicated pion selection algorithm (triangles), corresponding to the method 2 selection criterion. The indicated uncertainties are statistical.

D. Background subtraction summary

Figure 5(a) shows the $\chi^2_{4\pi}$ distribution both for the data after background subtraction and the signal simulation. Compared to Fig. 1(a), the difference between the data and the signal simulation is reduced. There is still some remaining background at larger $\chi^2_{4\pi}$ values as can be seen in Fig. 5(b). This is consistent with the uncertainties in the background-subtraction methods as previously described. To be conservative, we assume that the remaining background is uniform as a function of $\chi^2_{4\pi}$. In this case, we find that the associated uncertainty on the cross section is less
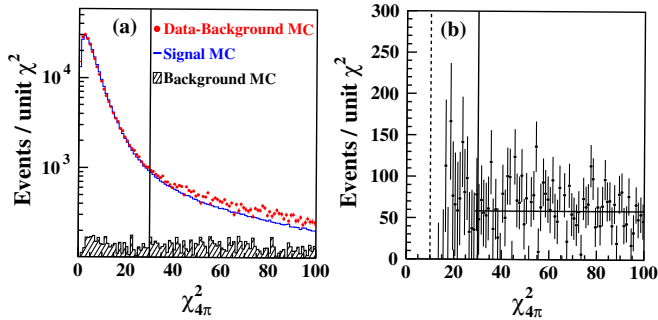

FIG. 5 (color online). (a) The χ^2 distribution for data after background subtraction (points), signal MC (histogram) and the sum of simulated background channels (hatched histogram). (b) The difference between data with background subtraction and signal MC. The dashed line indicates the boundary with the $0 < \chi^2_{4\pi} < 10$ region used for normalization.

than 0.4% for $M_{4\pi} < 2.8$ GeV/c^2 and 4.0% for 2.8 GeV/$c^2 < M_{4\pi} < 4.5$ GeV/c^2.

V. ACCEPTANCE AND EFFICIENCIES

The full chain of experimental requirements is applied to the signal MC sample. We define the ratio of the number of selected events divided by the number of events without applying any requirements as the global efficiency. Figure 6 shows the global efficiency as a function of $M_{4\pi}$ determined with the simulation. The decrease of efficiency in the threshold region, which corresponds to the highest energy ISR photons, is due to the fact that the four tracks of the hadronic system recoil in a narrow cone opposite to the direction of the ISR photon. Since ISR photons are preferentially emitted at small polar angles, the efficiency for detecting all four tracks within the fiducial volume of the detector decreases accordingly. The decrease in the global efficiency at large values of $M_{4\pi}$ can be explained with similar arguments, because the opening angle of the hadronic system increases with decreasing ISR photon energy, increasing the probability of losing one of the four tracks. The discontinuity at $M_{4\pi} = 1.1$ GeV/c^2 is due to the pion PID requirement for the tracks at low invariant masses.

As mentioned in section II, it is assumed that the $\pi^+\pi^-\pi^+\pi^-\gamma$ hadronic final state arises from the decay of various intermediate resonances such as $a_1(1260)\pi$. The relative contributions of intermediate states are discussed in Sec. VII. Different intermediate states might exhibit different results for the angular distributions of final-state particles. The limited knowledge of the hadronic substructure hence corresponds to a systematic uncertainty in the
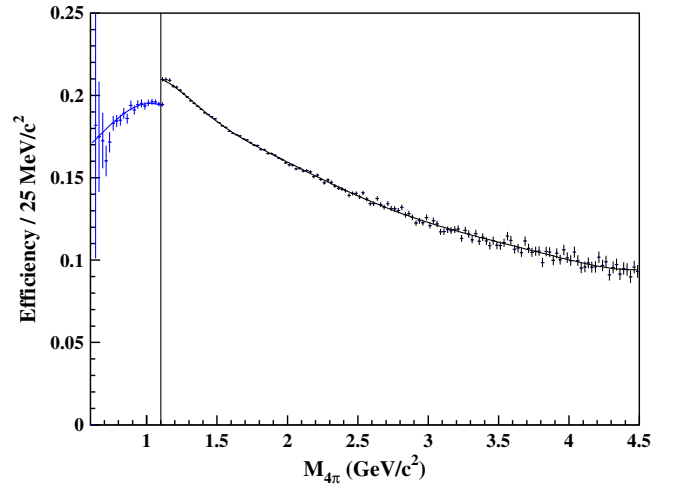

FIG. 6 (color online). The efficiency as a function of the $\pi^+\pi^-\pi^+\pi^-$ invariant mass. The vertical line at $M_{4\pi} = 1.1$ GeV/c^2 separates the regions with and without a pion PID requirement for the reconstructed tracks. The curves on either side of the vertical line are fits based on the sum of a Gaussian and a polynomial.

evaluation of the global efficiency. This effect is estimated through comparison of the predictions from AFKQED and a new version of PHOKHARA [16], which contain different intermediate resonances. The effect is observed to be negligible.

A. Photon efficiency

A dedicated study is performed to determine the photon efficiency in data and simulation. Detector inefficiencies due to inactive material between crystals, nonfunctioning crystals, and conversions in inner detector structures are investigated. This study is performed with a $\mu^+ \mu^- \gamma_{\rm ISR}$ sample, in which an identified ISR photon is not required in the event selection. A kinematic fit with one constraint (1C) based on the kinematic information of the charged tracks is performed in order to calculate the energy and direction of the photon. This fit prediction is compared to the measured photon information to extract the inefficiency of the photon reconstruction. In Fig. 7, the photon inefficiency is shown as a function of the polar angle of the photon for the data and simulation. The inefficiency curve is not smooth due to the effect of the inactive regions between EMC crystal rings. Some gaps between rings, which are visible in the data as peaks of high inefficiency, are not properly simulated, especially in the forward region of the detector. As a function of $M_{4\pi}$, we observe a uniform inefficiency difference between the data and the simulation with an average value of $\Delta\epsilon_\gamma = (1.34 \pm 0.03_{\rm stat} \pm 0.37_{\rm syst})\%$.
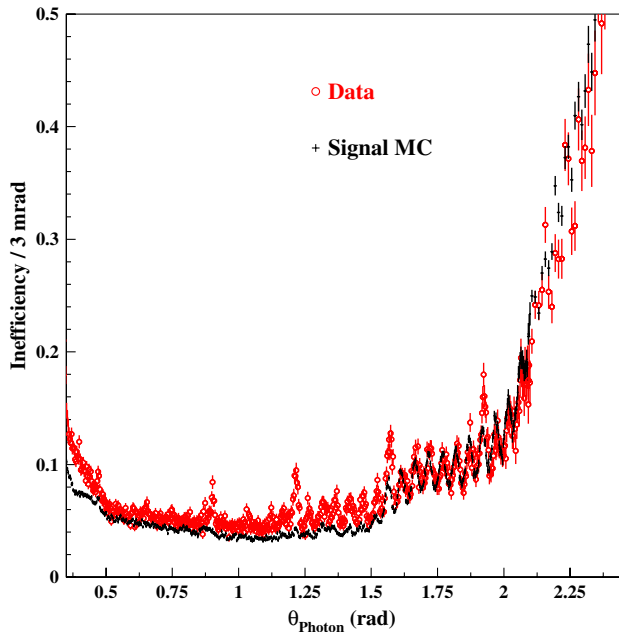

FIG. 7 (color online). Photon inefficiency as a function of the ISR photon polar angle for the data (circles) and signal MC (crosses). The binsize is increased to 6 mrad for $\theta_{\rm Photon} > 2.1$ rad.

B. Tracking efficiency

Track reconstruction and effects like nuclear interactions and energy loss of tracks traversing the detector volume are not simulated perfectly. As a consequence, the tracking efficiency is slightly different for the data and MC. This difference is investigated with a dedicated study of ISR $e^+ e^- \rightarrow \pi^+ \pi^- \pi^+ \pi^-$ events with one missing track. The missing momentum and direction of the lost pion is calculated using a constrained kinematic fit with one remaining constraint (1C). The angular and momentum dependent distribution of the inefficient events is extracted.

Small differences in tracking efficiency between the data and simulation are due to an imperfect description of track loss when tracks overlap in azimuth. The average difference between the data and MC is uniform as a function of the transverse momentum and the polar angle of the tracks and is determined on average to be $\Delta\epsilon_{\rm trk} = (0.75 \pm 0.05_{\rm stat} \pm 0.34_{\rm syst})\%$.

VI. CROSS SECTION

As described in Sec. I, the nonradiative cross section is related to the radiative cross section according to

$$\sigma_{4\pi}(M_{4\pi}) = \frac{d\sigma_{4\pi,\gamma}(M_{4\pi})}{dM_{4\pi}} \cdot \frac{s}{2M_{4\pi}} \cdot \frac{1}{W(s, x, C^*)}. \quad (2)$$

The radiative cross section is

$$\frac{d\sigma_{4\pi,\gamma}(M_{4\pi})}{dM_{4\pi}} = \frac{dN_{4\pi,\gamma}(M_{4\pi})}{dM_{4\pi}} \cdot \frac{1}{\mathcal{L}_{\rm tot} \cdot \epsilon \cdot (1 + \delta_{\rm rad,FSR})} \quad (3)$$

where $dN_{4\pi,\gamma}$ is the number of selected events, ϵ the global efficiency corrected for tracking and photon efficiency differences between the data and MC, and $\delta_{\rm rad,FSR}$ the radiative corrections including LO- and NLO-FSR effects. The MC event generator interfaced with the detector simulation is based on a modified version of the EVA code [22]. It contains collinear NLO-ISR corrections based on the structure function technique, as well as FSR corrections based on PHOTOS [27]. Radiative corrections due to NLO-ISR on the radiator function obtained with this event generator are compared to the PHOKHARA generator [16], which includes the full NLO-ISR corrections. With our selection, a $(1.0 \pm 0.2)\%$ difference of the radiator function between the two generators is observed. We apply a correction to account for this difference.

Figure 8 shows the ratio of the simulated ISR radiative cross section and the cross section including additional FSR (PHOTOS). The FSR leads to a shift of events towards lower invariant masses in the radiative cross section, due to the fact that the measured invariant mass is smaller than the effective $E_{\rm CM}$ for events with FSR.

After applying all radiative corrections and accounting for the relevant differences in efficiencies between the data and simulation, we apply Eq. (2) and extract the
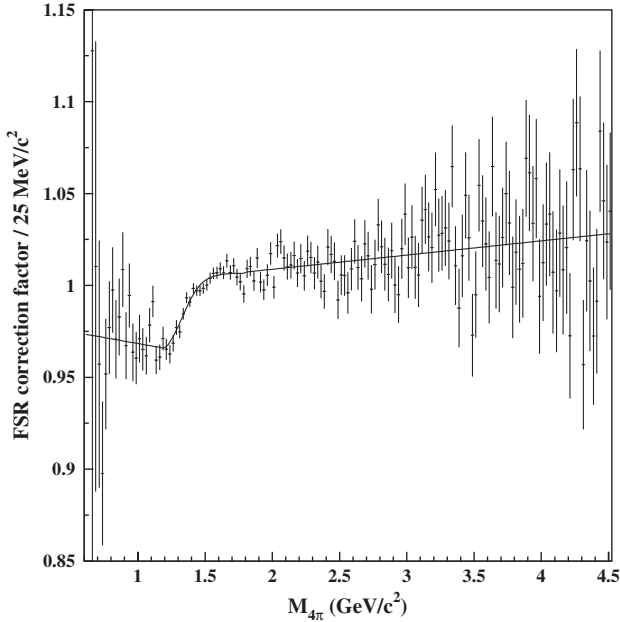
FIG. 8. Ratio of the simulated radiative cross section with only the ISR contribution to the cross section with both ISR and FSR.

nonradiative $e^+e^- \to \pi^+\pi^-\pi^+\pi^-$ cross section. The result is shown in Fig. 9. The measured cross section includes the contributions of vacuum polarization. The cross section used in the dispersion integral for a_μ does not include vacuum polarization and thus we need to apply a correction. We define the *undressed* cross section $\sigma_{4\pi}^{ud}(E_{CM})$ by
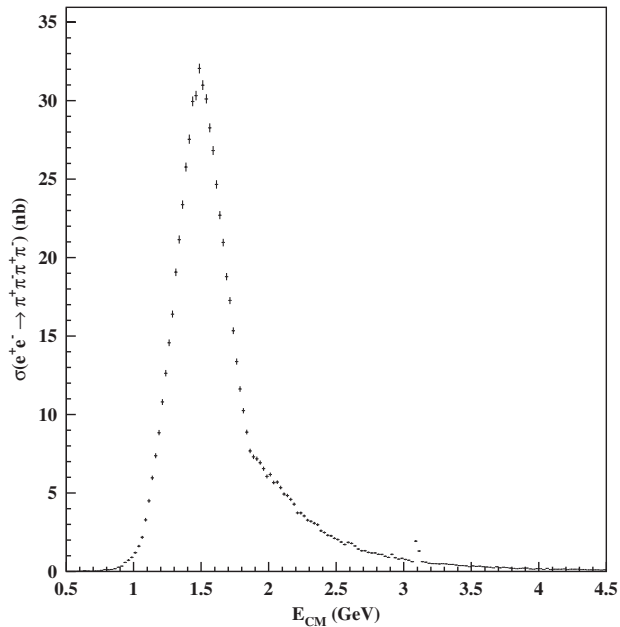

FIG. 9. The E_{CM} dependence of the dressed $e^+e^- \to \pi^+\pi^-\pi^+\pi^-$ cross section measured from the ISR data. The uncertainties are statistical.

correcting the measured or *dressed* cross section $\sigma_{4\pi}^d(E_{CM})$ for vacuum polarization effects according to

$$\sigma_{4\pi}^{ud}(E_{CM}) = \sigma_{4\pi}^d(E_{CM}) \cdot \left(\frac{\alpha(0)}{\alpha(E_{CM})}\right)^2 = \frac{\sigma_{4\pi}^d(E_{CM})}{\delta_{vac}(E_{CM})} \quad (4)$$

where $\alpha(E_{CM})$ is the electroweak coupling strength at E_{CM}. The correction due to vacuum polarization $\delta_{vac}(E_{CM})$, which can be found in Ref. [32], is applied. Our results for the dressed and the undressed cross sections are presented in Table I.

A. Systematic corrections and uncertainties

Table II presents the complete list of corrections and systematic uncertainties that are included in the dressed cross section. The uncertainties associated with background subtraction are discussed in Sec. IV. The 3.0% tracking efficiency difference between data and MC has an uncertainty of 1.4%. The photon efficiency correction is $1.3 \pm 0.4\%$. The total luminosity is measured with a precision of 1.0%. A $1.0 \pm 0.2\%$ difference is observed between the radiator functions computed with AFKQED and PHOKHARA. The effect of additional FSR is estimated using PHOTOS, resulting in the correction shown in Fig. 8 and a systematic uncertainty of 0.5%. The requirement $\chi_{4\pi}^2 < 30$ leads to a systematic uncertainty of 0.3%. The uncertainty on the global efficiency is estimated to be 1.0% in the central region, increasing to 10% in the low mass region $M_{4\pi} < 1.1$ GeV/c^2 due to an observed efficiency decrease of up to 10%. A conservative uncertainty of 10% to account for the total acceptance decrease in this region is also applied.

Assuming no correlation between the various contributions to the systematic uncertainty of the cross section, its total is found to be 10.7% for $M_{4\pi} < 1.1$ GeV/c^2, 2.4% for 1.1 GeV/$c^2 < M_{4\pi} < 2.8$ GeV/c^2, 5.5% for 2.8 GeV/$c^2 < M_{4\pi} < 4.0$ GeV/c^2 and 8.5% for higher invariant masses. Individual contributions to the systematic uncertainties contribute in a correlated way on the whole mass range, with the exception of the global analysis efficiency, for which it does not. Therefore for $M_{4\pi} > 1.1$ GeV/c^2 a 100% correlation can be assumed, while for $M_{4\pi} < 1.1$ GeV/c^2 where the global efficiency dominates, it can be assumed to be uncorrelated.

B. Comparison with the existing e^+e^- data

In Fig. 10 the extracted nonradiative $\sigma(e^+e^- \to \pi^+\pi^-\pi^+\pi^-)$ cross section is shown, in comparison with the previous *BABAR* result [8] and the results from fixed-energy e^+e^- experiments. Our results agree within the uncertainties with our previous measurement, which they supersede. Our results are consistent with and higher in precision than the direct e^+e^- cross section measurements made at VEPP-2M by OLYA [33], ND [34], SND [35], CMD [36], and CMD-2 [37–39], at DCI by M3N [40], DM1 [41], and DM2 [42], and at Adone by GG2 [43].

TABLE I. Summary of $e^+e^- \to \pi^+\pi^-\pi^+\pi^-$ cross section measurement. *Dressed* (with VP) and *undressed* (without VP) cross sections are presented with statistical uncertainties only.

E_{CM} (MeV)	$\sigma_{4\pi}^{dressed}$ (nb)	$\sigma_{4\pi}^{undressed}$ (nb)	E_{CM} (MeV)	$\sigma_{4\pi}^{dressed}$ (nb)	$\sigma_{4\pi}^{undressed}$ (nb)	E_{CM} (MeV)	$\sigma_{4\pi}^{dressed}$ (nb)	$\sigma_{4\pi}^{undressed}$ (nb)
612.5	0.02 ± 0.01	0.02 ± 0.01	1912.5	7.17 ± 0.14	6.90 ± 0.13	3212.5	0.50 ± 0.03	0.47 ± 0.03
637.5	0.04 ± 0.02	0.04 ± 0.02	1937.5	6.93 ± 0.13	6.67 ± 0.13	3237.5	0.49 ± 0.03	0.46 ± 0.03
662.5	0.02 ± 0.01	0.02 ± 0.01	1962.5	6.54 ± 0.13	6.30 ± 0.13	3262.5	0.48 ± 0.03	0.45 ± 0.03
687.5	0.01 ± 0.01	0.01 ± 0.01	1987.5	6.04 ± 0.12	5.82 ± 0.12	3287.5	0.49 ± 0.03	0.47 ± 0.03
712.5	0.02 ± 0.01	0.02 ± 0.01	2012.5	6.18 ± 0.13	5.95 ± 0.12	3312.5	0.47 ± 0.03	0.45 ± 0.03
737.5	0.03 ± 0.01	0.03 ± 0.01	2037.5	5.66 ± 0.12	5.45 ± 0.12	3337.5	0.44 ± 0.03	0.42 ± 0.03
762.5	0.05 ± 0.02	0.05 ± 0.02	2062.5	5.68 ± 0.12	5.47 ± 0.12	3362.5	0.44 ± 0.03	0.42 ± 0.03
787.5	0.11 ± 0.03	0.10 ± 0.02	2087.5	5.34 ± 0.12	5.14 ± 0.11	3387.5	0.40 ± 0.03	0.38 ± 0.03
812.5	0.11 ± 0.02	0.10 ± 0.02	2112.5	4.92 ± 0.11	4.73 ± 0.11	3412.5	0.38 ± 0.03	0.36 ± 0.03
837.5	0.12 ± 0.03	0.12 ± 0.02	2137.5	4.83 ± 0.11	4.64 ± 0.11	3437.5	0.38 ± 0.03	0.36 ± 0.03
862.5	0.17 ± 0.03	0.16 ± 0.03	2162.5	4.59 ± 0.11	4.41 ± 0.10	3462.5	0.36 ± 0.03	0.34 ± 0.02
887.5	0.26 ± 0.04	0.25 ± 0.03	2187.5	4.28 ± 0.10	4.12 ± 0.10	3487.5	0.30 ± 0.02	0.28 ± 0.02
912.5	0.33 ± 0.04	0.32 ± 0.04	2212.5	3.72 ± 0.10	3.58 ± 0.09	3512.5	0.35 ± 0.03	0.33 ± 0.02
937.5	0.57 ± 0.05	0.55 ± 0.05	2237.5	3.72 ± 0.09	3.57 ± 0.09	3537.5	0.31 ± 0.02	0.29 ± 0.02
962.5	0.71 ± 0.06	0.69 ± 0.05	2262.5	3.53 ± 0.09	3.39 ± 0.09	3562.5	0.33 ± 0.02	0.31 ± 0.02
987.5	0.89 ± 0.06	0.86 ± 0.06	2287.5	3.26 ± 0.09	3.13 ± 0.08	3587.5	0.29 ± 0.02	0.28 ± 0.02
1012.5	1.20 ± 0.07	1.23 ± 0.07	2312.5	3.18 ± 0.09	3.06 ± 0.08	3612.5	0.27 ± 0.02	0.26 ± 0.02
1037.5	1.61 ± 0.08	1.51 ± 0.08	2337.5	3.06 ± 0.08	2.94 ± 0.08	3637.5	0.26 ± 0.02	0.25 ± 0.02
1062.5	2.17 ± 0.09	2.06 ± 0.09	2362.5	2.97 ± 0.08	2.86 ± 0.08	3662.5	0.22 ± 0.02	0.22 ± 0.02
1087.5	3.29 ± 0.11	3.14 ± 0.11	2387.5	2.59 ± 0.08	2.48 ± 0.07	3687.5	0.29 ± 0.02	0.13 ± 0.02
1112.5	4.49 ± 0.13	4.31 ± 0.12	2412.5	2.47 ± 0.08	2.38 ± 0.07	3712.5	0.23 ± 0.02	0.21 ± 0.02
1137.5	5.95 ± 0.14	5.72 ± 0.14	2437.5	2.30 ± 0.07	2.21 ± 0.07	3737.5	0.26 ± 0.02	0.24 ± 0.02
1162.5	7.37 ± 0.16	7.09 ± 0.15	2462.5	2.25 ± 0.07	2.16 ± 0.07	3762.5	0.25 ± 0.02	0.23 ± 0.02
1187.5	8.84 ± 0.17	8.51 ± 0.17	2487.5	2.11 ± 0.07	2.02 ± 0.07	3787.5	0.21 ± 0.02	0.20 ± 0.02
1212.5	10.79 ± 0.19	10.40 ± 0.18	2512.5	2.03 ± 0.07	1.95 ± 0.07	3812.5	0.19 ± 0.02	0.18 ± 0.02
1237.5	12.62 ± 0.20	12.17 ± 0.20	2537.5	1.87 ± 0.07	1.80 ± 0.06	3837.5	0.18 ± 0.02	0.17 ± 0.02
1262.5	14.56 ± 0.22	14.05 ± 0.21	2562.5	1.71 ± 0.06	1.65 ± 0.06	3862.5	0.18 ± 0.02	0.17 ± 0.02
1287.5	16.39 ± 0.23	15.83 ± 0.22	2587.5	1.85 ± 0.06	1.77 ± 0.06	3887.5	0.21 ± 0.02	0.20 ± 0.02
1312.5	19.06 ± 0.25	18.41 ± 0.24	2612.5	1.79 ± 0.06	1.72 ± 0.06	3912.5	0.20 ± 0.02	0.19 ± 0.02
1337.5	21.14 ± 0.26	20.42 ± 0.25	2637.5	1.62 ± 0.06	1.56 ± 0.06	3937.5	0.15 ± 0.02	0.14 ± 0.02
1362.5	23.37 ± 0.27	22.59 ± 0.26	2662.5	1.43 ± 0.06	1.37 ± 0.05	3962.5	0.14 ± 0.02	0.14 ± 0.01
1387.5	25.76 ± 0.28	24.90 ± 0.28	2687.5	1.31 ± 0.05	1.26 ± 0.05	3987.5	0.16 ± 0.02	0.16 ± 0.02
1412.5	27.53 ± 0.29	26.61 ± 0.29	2712.5	1.30 ± 0.05	1.26 ± 0.05	4012.5	0.17 ± 0.02	0.16 ± 0.02
1437.5	29.95 ± 0.30	28.96 ± 0.30	2737.5	1.21 ± 0.05	1.16 ± 0.05	4037.5	0.12 ± 0.01	0.11 ± 0.01
1462.5	30.32 ± 0.31	29.32 ± 0.30	2762.5	1.17 ± 0.05	1.13 ± 0.05	4062.5	0.20 ± 0.02	0.19 ± 0.02
1487.5	32.04 ± 0.31	30.97 ± 0.30	2787.5	1.17 ± 0.05	1.12 ± 0.05	4087.5	0.13 ± 0.01	0.12 ± 0.01
1512.5	30.98 ± 0.31	29.93 ± 0.30	2812.5	1.09 ± 0.05	1.05 ± 0.05	4112.5	0.14 ± 0.02	0.13 ± 0.01
1537.5	30.11 ± 0.30	29.06 ± 0.29	2837.5	1.07 ± 0.05	1.04 ± 0.05	4137.5	0.14 ± 0.02	0.13 ± 0.01
1562.5	28.26 ± 0.29	27.26 ± 0.28	2862.5	0.96 ± 0.05	0.93 ± 0.04	4162.5	0.14 ± 0.01	0.13 ± 0.01
1587.5	26.81 ± 0.28	25.86 ± 0.27	2887.5	0.89 ± 0.04	0.86 ± 0.04	4187.5	0.15 ± 0.02	0.14 ± 0.01
1612.5	24.66 ± 0.27	23.78 ± 0.26	2912.5	1.08 ± 0.05	1.05 ± 0.05	4212.5	0.11 ± 0.01	0.10 ± 0.01
1637.5	22.69 ± 0.26	21.89 ± 0.25	2937.5	0.88 ± 0.04	0.85 ± 0.04	4237.5	0.13 ± 0.01	0.12 ± 0.01
1662.5	20.95 ± 0.25	20.19 ± 0.24	2962.5	0.77 ± 0.04	0.75 ± 0.04	4262.5	0.13 ± 0.01	0.12 ± 0.01
1687.5	18.78 ± 0.23	18.09 ± 0.22	2987.5	0.82 ± 0.04	0.81 ± 0.04	4287.5	0.13 ± 0.01	0.12 ± 0.01
1712.5	17.25 ± 0.22	16.61 ± 0.21	3012.5	0.75 ± 0.04	0.74 ± 0.04	4312.5	0.11 ± 0.01	0.11 ± 0.01
1737.5	15.33 ± 0.21	14.75 ± 0.20	3037.5	0.71 ± 0.04	0.71 ± 0.04	4337.5	0.11 ± 0.01	0.11 ± 0.01
1762.5	13.37 ± 0.19	12.86 ± 0.19	3062.5	0.62 ± 0.04	0.66 ± 0.04	4362.5	0.09 ± 0.01	0.09 ± 0.01
1787.5	11.61 ± 0.18	11.17 ± 0.17	3087.5	1.93 ± 0.06	2.30 ± 0.08	4387.5	0.10 ± 0.01	0.10 ± 0.01
1812.5	10.23 ± 0.17	9.84 ± 0.16	3112.5	1.30 ± 0.05	1.03 ± 0.04	4412.5	0.11 ± 0.01	0.10 ± 0.01
1837.5	8.87 ± 0.15	8.53 ± 0.15	3137.5	0.62 ± 0.04	0.55 ± 0.03	4437.5	0.09 ± 0.01	0.09 ± 0.01
1862.5	7.67 ± 0.14	7.37 ± 0.14	3162.5	0.59 ± 0.03	0.54 ± 0.03	4462.5	0.09 ± 0.01	0.08 ± 0.01
1887.5	7.29 ± 0.14	7.02 ± 0.13	3187.5	0.51 ± 0.03	0.47 ± 0.03	4487.5	0.10 ± 0.01	0.09 ± 0.01

TABLE II. Summary of systematic corrections and uncertainties in per centage.

$M_{4\pi}$	<1.1 GeV/c^2	<2.8 GeV/c^2	<4.0 GeV/c^2	<4.5 GeV/c^2
$K^+ K^- \pi^+ \pi^- \gamma$, $K_S^0 K^\pm \pi^\mp \gamma$	± 1.0	± 1.0	± 3.0	± 7.0
continuum bkg	$-$	± 0.5	± 1.0	± 1.5
$\pi^+ \pi^- e^+ e^- \gamma$	± 3.0	$-$	$-$	$-$
additional bkg	± 0.4	± 0.4	± 4.0	± 4.0
tracking efficiency	$+3.0 \pm 1.4$	$+3.0 \pm 1.4$	$+3.0 \pm 1.4$	$+3.0 \pm 1.4$
photon efficiency	$+1.3 \pm 0.4$	$+1.3 \pm 0.4$	$+1.3 \pm 0.4$	$+1.3 \pm 0.4$
$\mathcal{L}$	± 1.0	± 1.0	± 1.0	± 1.0
AFK-PHOK-difference	-1.0 ± 0.2	-1.0 ± 0.2	-1.0 ± 0.2	-1.0 ± 0.2
FSR corrections	± 0.5	± 0.2	± 0.1	± 0.1
$\chi^2_{4\pi} < 30$	± 0.3	± 0.3	± 0.3	± 0.3
global efficiency	± 10.0	± 1.0	± 1.0	± 1.0
sum	± 10.7	± 2.4	± 5.5	± 8.5

C. Influence on the prediction of a_μ

Using the result for the $e^+ e^- \to \pi^+ \pi^- \pi^+ \pi^-$ cross section obtained in the present study, we compute the contribution of this channel to the anomalous magnetic moment of the muon a_μ via a dispersion relation using the HVPTool program [44] in the energy region 0.6 GeV$<$ $E_{CM} < 1.8$ GeV. We find

$$a_\mu^{had}(\pi^+ \pi^- \pi^+ \pi^-) = (13.64 \pm 0.03_{stat} \pm 0.36_{syst}) \times 10^{-10}.$$
(5)

Our result is more precise than the current world average for this quantity: $(13.35 \pm 0.10_{stat} \pm 0.52_{syst}) \times 10^{-10}$
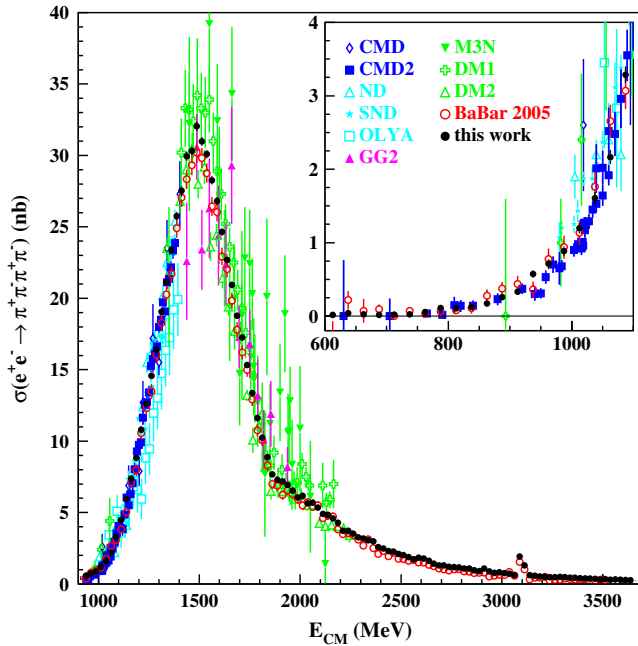

FIG. 10 (color online). The $e^+ e^- \to \pi^+ \pi^- \pi^+ \pi^-$ cross section in comparison to other experiments. Only statistical uncertainties are shown.

[19], where the first uncertainty is statistical and the second systematic.

VII. INVARIANT MASSES AND CHARMONIUM BRANCHING RATIOS

Different invariant mass combinations have been studied in the data and MC simulation to search for states not included in the MC model. In the following, we present a general qualitative search for these hadronic structures. We then consider a more detailed study of the J/ψ and $\psi(2S)$ background subtraction and efficiency corrections. Finally, we determine the branching fractions $\mathcal{B}_{J/\psi \to \pi^+ \pi^- \pi^+ \pi^-}$ and $\mathcal{B}_{\psi(2S) \to J/\psi \pi^+ \pi^-}$ and perform a scan for additional resonances at high invariant masses.

A. Substructures

The scatter plots in Fig. 11 display distributions of the invariant $\pi^+ \pi^- \pi^\pm$ and $\pi^+ \pi^-$ masses versus the invariant $\pi^+ \pi^- \pi^+ \pi^-$ mass for the data and MC. The $\rho(770)^0$ band is clearly visible in the $\pi^+ \pi^-$ mass distribution of the data and MC. In general, good agreement is seen except for the J/ψ decay, which is not simulated.

In a more detailed study, the $\pi^+ \pi^- \pi^+ \pi^-$ mass spectrum is divided into five intervals:
(1) 1.0–1.4 GeV/c^2: low mass region
(2) 1.4–1.8 GeV/c^2: peak region of the cross section
(3) 1.8–2.3 GeV/c^2: high mass shoulder
(4) 2.3–3.0 GeV/c^2
(5) 3.0–4.5 GeV/c^2: without the narrow region around J/ψ

Figure 12 shows the one-dimensional distributions from the five regions for the two- and three-pion invariant masses in comparison with MC [22].

The $\pi^+ \pi^- \pi^\pm$ invariant mass distribution is shown in the leftmost column of Fig. 12. In the low mass region, 1.0 GeV/$c^2 < M_{4\pi} < 1.4$ GeV/c^2, there is not enough energy to allow production of the $a_1(1260)^\pm$. At higher
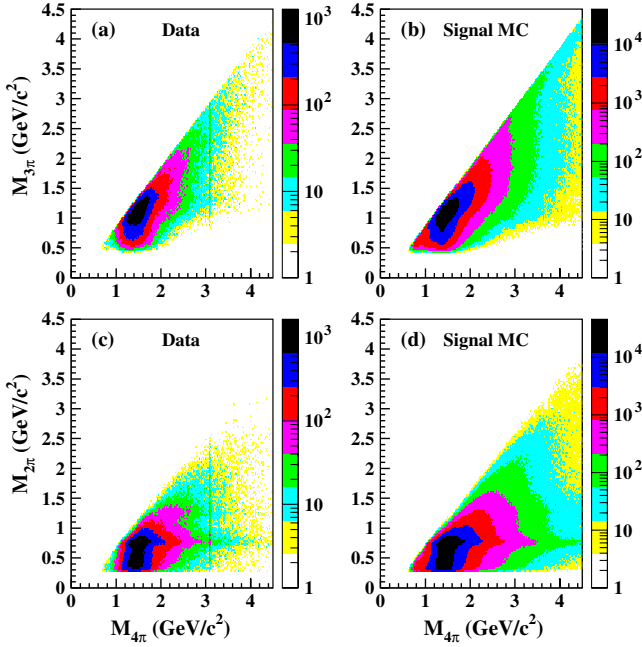
FIG. 11 (color online). Invariant $\pi^+\pi^-\pi^\pm$ and $\pi^+\pi^-$ mass combinations vs invariant $\pi^+\pi^-\pi^+\pi^-$ mass for the data without background subtraction (left) and signal MC (right).

$M_{4\pi}$, the contribution of the $a_1(1260)^\pm$ becomes visible. It is observed as a peaking structure with mass and width $M_{3\pi} \approx 1300$ MeV/c^2 and $\Gamma \approx 200$ MeV. In comparison, the average mass value in the PDG [31] is 1.230 ± 0.040 GeV/c^2, with results from individual experiments that vary between 1.04 and 1.33 GeV/c^2. The corresponding width varies between 250 and 600 MeV. In our simulation, the parameters $M = 1.33$ GeV/c^2 and $\Gamma = 570$ MeV are used, which are determined from a combined analysis of the CLEO and CMD-2 data [24]. Our results seem to favor a lower $a_1(1260)^\pm$ mass and a smaller width.

In the $\pi^+\pi^-$ invariant mass distributions shown in the middle column of Fig. 12, four entries are present per event. At low 4π mass and in the peak region only a single resonance, the $\rho(770)^0$, is observed. At larger 4π mass, a second peaking structure appears at $M_{2\pi} \approx 1270$ MeV/c^2, which most likely corresponds to the $f_2(1270)$. This resonance is not simulated by our MC. It is observed that over the entire 4π mass range, approximately 25% of the entries are in the $\rho(770)^0$ peak. $\rho(770)^0\rho(770)^0$ production is not allowed due to C-parity conservation, leading to the conclusion that in each event one $\rho(770)^0$ meson is present.

To investigate the possible presence of the $f_2(1270)\rho(770)^0$ final state, the $\pi^+\pi^-$ combination is plotted for the case that there is another $\pi^+\pi^-$ combination within ± 25 MeV/c^2 of the $\rho(770)^0$ mass, 745 MeV/$c^2 < M_{2\pi} < 795$ MeV/c^2. The results are shown in the rightmost column of Fig. 12. An artificial dip at $M_{2\pi} \approx 770$ MeV/c^2 due to the selection of the $\rho(770)^0$ is observed. The $f_2(1270)$ resonance is visible as a shoulder in

the 1.8 GeV/$c^2 < M_{4\pi} < 2.3$ GeV/c^2 mass region. It is even more prominent in the 2.3 GeV/$c^2 < M_{4\pi} < 4.5$ GeV/c^2 region, where the energy is large enough to allow direct production of $f_2(1270)\rho(770)^0$. A sharp falloff in the $M_{2\pi}$ spectrum just below 1 GeV/c^2 is visible in the 1.8 GeV/$c^2 < M_{4\pi} < 2.3$ GeV/c^2 region. This might be due to interference with the $f_0(980)$ final state. A partial wave analysis, which is beyond the scope of this paper, would be necessary to determine the structure of the individual intermediate states. A qualitative comparison with the MC model of Ref. [16] indicates a somewhat better agreement with the data than that shown in the rightmost column of Fig. 12, apart from an overestimate of the contribution of the $f_0(1300)\rho(770)^0$ final state.

B. J/ψ and $\psi(2S)$

Figure 13(a) displays the $\sigma(e^+e^- \to \pi^+\pi^-\pi^+\pi^-)$ cross section as a function of the 4π mass, in the vicinity of the J/ψ meson. The measured width of the J/ψ (≈ 15 MeV) is dominated by the track momentum resolution, the intrinsic width being $\Gamma_{J/\psi} = 93$ keV [31]. The small tail toward higher masses is mostly from extra radiation, which is assigned to the hadronic system by the fit. We describe the J/ψ peak and the nonresonant $\pi^+\pi^-\pi^+\pi^-$ contribution with the sum of two Gaussians and a linear term, respectively. This allows the integrated partial cross section $\sigma_{\mathrm{int}}^{J/\psi} = \int_0^\infty dM_{4\pi}\sigma^{J/\psi}(M_{4\pi})$ and the electronic width of $J/\psi \to \pi^+\pi^-\pi^+\pi^-$ to be extracted:

$$
\begin{aligned}
\mathcal{B}_{J/\psi \to \pi^+\pi^-\pi^+\pi^-} &\cdot \sigma_{\mathrm{int}}^{J/\psi} \\
&= \frac{N(J/\psi \to \pi^+\pi^-\pi^+\pi^-)}{d\mathcal{L}/dE \cdot \epsilon_{\mathrm{MC}}} \\
&= (48.9 \pm 2.1_{\mathrm{stat}} \pm 1.0_{\mathrm{syst}}) \text{ MeV}/c^2 \text{ nb}
\end{aligned} \tag{6}
$$

and

$$
\begin{aligned}
\mathcal{B}_{J/\psi \to \pi^+\pi^-\pi^+\pi^-} \cdot \Gamma_{ee}^{J/\psi} &= \frac{N(J/\psi \to \pi^+\pi^-\pi^+\pi^-) \cdot M_{J/\psi}^2}{6\pi^2 \cdot d\mathcal{L}/dE \cdot \epsilon_{\mathrm{MC}} \cdot C} \\
&= (20.4 \pm 0.9_{\mathrm{stat}} \pm 0.4_{\mathrm{syst}}) \text{ eV}.
\end{aligned} \tag{7}
$$

For the above, the value $M_{J/\psi} = 3096.92 \pm 0.01$ MeV/c^2 [31] and the conversion constant $C = 3.8938 \times 10^{11}$ MeV^2 nb [31] are used. The statistical uncertainty corresponds to the fit uncertainty on the area under the two Gaussian distributions, which is a fit parameter. A systematic uncertainty of 3% covers the systematic effects related to the luminosity and efficiencies. Contributions from background that peak at the J/ψ mass are negligible. Using the electronic width $\Gamma_{ee}^{J/\psi} = 5.55 \pm 0.14$ keV, we determine the $J/\psi \to \pi^+\pi^-\pi^+\pi^-$ branching fraction to be
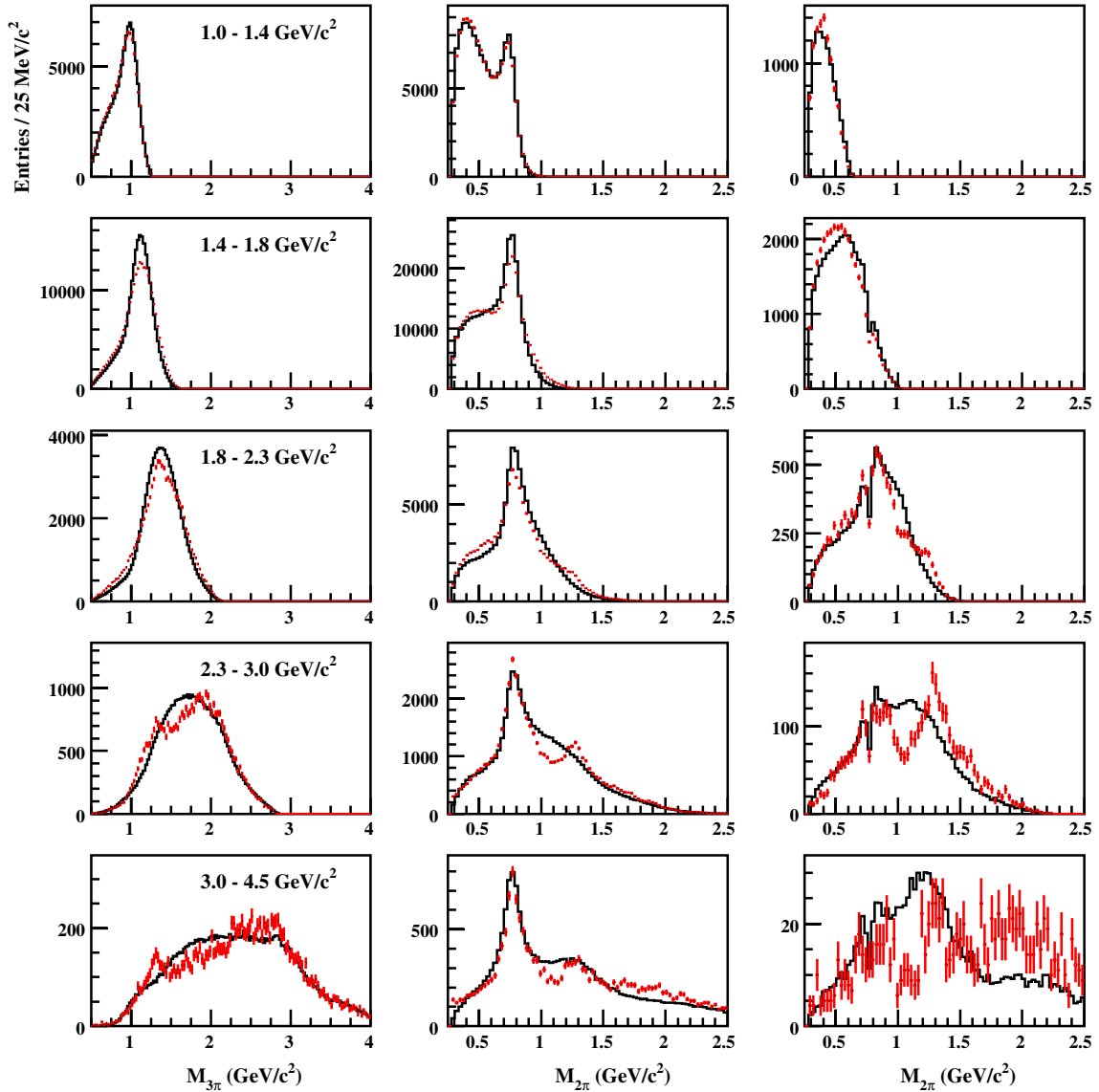
FIG. 12 (color online). Left: invariant $\pi^+\pi^-\pi^\pm$ mass distributions (four entries per event) for different regions in $M_{4\pi}$ for the data without background subtraction (points) and signal simulation (histogram); Middle: $\pi^+\pi^-$ mass distributions (4 entries per event); Right: $\pi^+\pi^-$ mass distribution with another $\pi^+\pi^-$ mass in the $\rho(770)^0$ mass region.

$$\mathcal{B}_{J/\psi \rightarrow \pi^+\pi^-\pi^+\pi^-}$$
$$= (3.67 \pm 0.16_{\text{stat}} \pm 0.08_{\text{syst}} \pm 0.09_{\text{ext}}) \times 10^{-3}. \qquad (8)$$

The external uncertainty (denoted *ext*) is dominated by the uncertainty of $\Gamma_{ee}^{J/\psi}$ [31]. This measurement agrees with the current PDG [31] value $(3.55 \pm 0.23) \times 10^{-3}$.

A clear $\psi(2S) \rightarrow \pi^+\pi^-\mu^+\mu^-$ peak in the data of Fig. 3(a) is visible. Because the selection efficiency for $\pi^+\pi^-\mu^+\mu^-$ is the same as for $\pi^+\pi^-\pi^+\pi^-$, we can extract the branching fraction $\mathcal{B}_{\psi(2S)\rightarrow J/\psi\pi^+\pi^-}$ with $J/\psi \rightarrow \mu^+\mu^-$ from a simple fit to the $\pi^+\pi^-\pi^+\pi^-$ mass distribution. Figure 13(b) shows the invariant mass distribution under the $\pi^+\pi^-\pi^+\pi^-$ hypothesis in the $\psi(2S)$ mass region.

The measured width of the $\psi(2S)$ (≈ 20 MeV) is, as in the case of the J/ψ, dominated by the track momentum

resolution, the intrinsic width of the $\psi(2S)$ being $\Gamma_\psi(2S) = 317$ keV [31]. The effect of using the π mass hypothesis in the μ track fit is negligible. The peak is described by the sum of two Gaussian distributions and the nonresonant $\pi^+\pi^-\pi^+\pi^-$ contribution with a linear function. The area under the peak is used to determine the $\psi(2S) \rightarrow J/\psi\pi^+\pi^-$ branching fraction according to the following equation:

$$\mathcal{B}_{\psi(2S)\rightarrow J/\psi\pi^+\pi^-} \cdot \mathcal{B}_{J/\psi\rightarrow\mu^+\mu^-} \cdot \sigma_{\text{int}}^{\psi(2S)}$$
$$= \frac{N(\psi(2S) \rightarrow \pi^+\pi^-\mu^+\mu^-)}{d\mathcal{L}/dE \cdot \epsilon_{\text{MC}}}$$
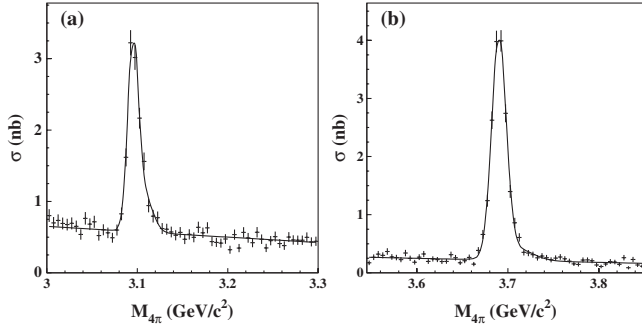$$= (84.7 \pm 2.2_{\text{stat}} \pm 1.8_{\text{syst}}) \text{ MeV}/c^2 \text{ nb} \qquad (9)$$

and

FIG. 13. (a) Invariant 4π mass $M_{4\pi}$ distribution for the data around the J/ψ peak with a fit, which consists of a sum of two Gaussian and a linear distribution, describing the peak and the nonresonant $\pi^+\pi^-\pi^+\pi^-$ contribution, respectively. (b) Invariant $\pi^+\pi^-\pi^+\pi^-$ mass $M_{4\pi}$ distribution, assuming all four particles are pions, for the data around the $\psi(2S)$ peak with a fit, which consists of a sum of two Gaussian and a linear distribution, describing the peak and the nonresonant $\pi^+\pi^-\pi^+\pi^-$ contribution, respectively.

$$\mathcal{B}_{\psi(2S)\to J/\psi\pi^+\pi^-} \cdot \mathcal{B}_{J/\psi\to\mu^+\mu^-} \cdot \Gamma_{ee}^{\psi(2S)}$$

$$= \frac{N(\psi(2S)\to\pi^+\pi^-\mu^+\mu^-) \cdot M_{\psi(2S)}^2}{6\pi^2 \cdot d\mathcal{L}/dE \cdot \epsilon_{\mathrm{MC}} \cdot C}$$

$$= (49.9 \pm 1.3_{\mathrm{stat}} \pm 1.0_{\mathrm{syst}}) \text{ eV}, \qquad (10)$$

where the latter result uses $M_{\psi(2S)} = 3686.09 \pm 0.04$ MeV/c^2 [31] and the conversion constant $C = 3.8938 \times 10^{11}$ MeV^2 nb [31]. The statistical uncertainty corresponds to the fit uncertainty on the area of the two Gaussian distributions and the systematic uncertainty of 3% covers the systematic uncertainties in the luminosity and efficiencies. Contributions from peaking background are negligible. The $\mathcal{B}_{J/\psi\to\mu^+\mu^-} = 0.0593 \pm 0.0006$ branching fraction is known with very high precision. Using $\Gamma_{ee}^{\psi(2S)} = (2.38 \pm 0.04)$ keV [31], the $\psi(2S) \to J/\psi\pi^+\pi^-$ branching fraction is determined to be

$$\mathcal{B}_{\psi(2S)\to J/\psi\pi^+\pi^-} = 0.354 \pm 0.009_{\mathrm{stat}} \pm 0.007_{\mathrm{syst}}$$

$$\pm 0.007_{\mathrm{ext}}, \qquad (11)$$

where the external uncertainty is dominated by the uncertainty for $\Gamma_{ee}^{\psi(2S)}$ [31]. The measurement is slightly higher than the PDG [31] value $\mathcal{B}_{\psi(2S)\to J/\psi\pi^+\pi^-} = 0.336 \pm 0.005$, but agrees within the uncertainties. Our result is comparable in precision to the individual results used to determine the PDG average and agrees well with the most recent CLEO measurement $\mathcal{B}_{\psi(2S)\to J/\psi\pi^+\pi^-} = 0.3504 \pm 0.0007 \pm 0.0077$ [45].

C. Scan for additional resonances

Figure 14(a) displays the $M_{4\pi}$ distribution for the data in the high invariant mass region. No clear signal can be
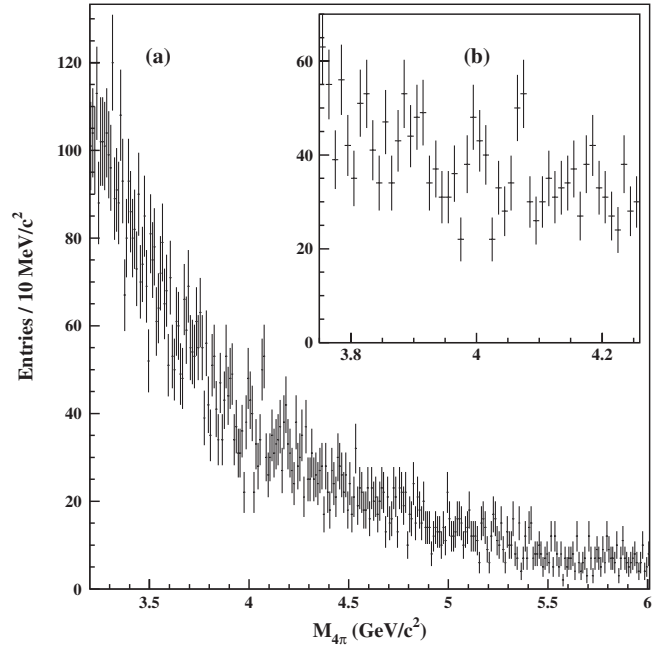

FIG. 14. Invariant $\pi^+\pi^-\pi^+\pi^-$ mass distribution for the data in the invariant mass range 3.2 GeV/$c^2 < M_{4\pi} < 6.0$ GeV/c^2 (a) and 3.75 GeV/$c^2 < M_{4\pi} < 4.25$ GeV/c^2 (inset, b).

identified. There is a hint of structure just above 4 GeV/c^2. The inset, Fig. 14(b), shows this feature in more detail.

VIII. SUMMARY

In this paper, we present a measurement of the $\pi^+\pi^-\pi^+\pi^-$ cross section at effective center-of-mass energies below 4.5 GeV, using e^+e^- events with ISR collected in the vicinity of the $\Upsilon(4S)$ resonance. We achieve overall uncertainties of 2.4% in the peak region defined by 1.1 GeV/$c^2 < M_{4\pi} < 2.2$ GeV/c^2, 10.7% below 1.1 GeV/c^2, 5.5% above 2.8 GeV/c^2 and 8.5% above 4.0 GeV/c^2. These cross section results are much more precise than the corresponding ones based on energy scans.

The resulting contribution of the $\sigma(e^+e^- \to \pi^+\pi^-\pi^+\pi^-)$ cross section to the anomalous magnetic moment of the muon $a_\mu^{\mathrm{had}}(e^+e^- \to \pi^+\pi^-\pi^+\pi^-)$ is evaluated according to the method described in Ref. [44] in the CM energy region between 0.6 and 1.8 GeV:

$$a_\mu^{\mathrm{had}}(\pi^+\pi^-\pi^+\pi^-) = (13.64 \pm 0.03_{\mathrm{stat}} \pm 0.36_{\mathrm{syst}}) \times 10^{-10}.$$

$$(12)$$

The cross section shows evidence of resonant substructure, with preferred quasi-two-body production of $a_1(1260)\pi$. There is an indication of a $f_2(1270)\rho(770)$ contribution to the final state. A detailed understanding of the four-pion final state requires additional information from states such as $\pi^+\pi^-\pi^0\pi^0$.

The ISR events allow a study of J/ψ and $\psi(2S)$ production. We measure the product of decay branching

fractions and the e^+e^- width of the J/ψ with the best accuracy to date, with the results

$$\mathcal{B}_{J/\psi \to \pi^+\pi^-\pi^+\pi^-} \cdot \Gamma_{ee}^{J/\psi} = (20.4 \pm 0.9_{\text{stat}} \pm 0.4_{\text{syst}}) \text{ eV} \tag{13}$$

$$\mathcal{B}_{\psi(2S) \to J/\psi \pi^+\pi^-} \cdot \mathcal{B}_{J/\psi \to \mu^+\mu^-} \cdot \Gamma_{ee}^{\psi(2S)}$$
$$= (49.9 \pm 1.3_{\text{stat}} \pm 1.0_{\text{syst}}) \text{ eV}. \tag{14}$$

ACKNOWLEDGMENTS

[1] N. Cabibbo and R. Gatto, Phys. Rev. Lett. **4**, 313 (1960); Phys. Rev. **124**, 1577 (1961).

[2] G. W. Bennett *et al.* (Muon $g - 2$ Collaboration), Phys. Rev. D **73**, 072003 (2006).

[3] A. B. Arbuzov *et al.*, J. High Energy Phys. 12 (1998) 009.

[4] S. Binner, J. H. Kühn, and K. Melnikov, Phys. Lett. B **459**, 279 (1999).

[5] M. Benayoun *et al.*, Mod. Phys. Lett. A **14**, 2605 (1999).

[6] V. P. Druzhinin, S. I. Eidelman, S. I. Serednyakov, and E. P. Solodov, Rev. Mod. Phys. **83**, 1545 (2011).

[7] B. Aubert *et al.* (*BABAR* Collaboration), Phys. Rev. D **70**, 072004 (2004).

[8] B. Aubert *et al.* (*BABAR* Collaboration), Phys. Rev. D **71**, 052001 (2005).

[9] B. Aubert *et al.* (*BABAR* Collaboration), Phys. Rev. D **73**, 052003 (2006).

[10] B. Aubert *et al.* (*BABAR* Collaboration), Phys. Rev. D **73**, 012005 (2006).

[11] B. Aubert *et al.* (*BABAR* Collaboration), Phys. Rev. D **76**, 092006 (2007).

[12] B. Aubert *et al.* (*BABAR* Collaboration), Phys. Rev. D **76**, 092005 (2007).

[13] B. Aubert *et al.* (*BABAR* Collaboration), Phys. Rev. D **76**, 012008 (2007).

[14] B. Aubert *et al.* (*BABAR* Collaboration), Phys. Rev. D **77**, 092002 (2008).

[15] B. Aubert *et al.* (*BABAR* Collaboration), Phys. Rev. Lett. **103**, 231801 (2009).

[16] H. Czyż, J. H. Kühn, and A. Wapienik, Phys. Rev. D **77**, 114005 (2008); H. Czyż, A. Grzelinska, and J. H. Kühn, Phys. Rev. D **81**, 094014 (2010), and references therein.

[17] F. Ambrosino *et al.* (KLOE Collaboration), Phys. Lett. B **700**, 102 (2011).

[18] F. Ambrosino *et al.* (KLOE Collaboration), Phys. Lett. B **669**, 223 (2008).

[19] M. Davier *et al.*, Eur. Phys. J. C **71**, 1515 (2011); **72**, 1874 (E) (2012).

[20] F. Jegerlehner and A. Nyffeler, Phys. Rep. **477**, 1 (2009).

[21] B. Aubert *et al.* (*BABAR* Collaboration), Nucl. Instrum. Methods Phys. Res., Sect. A **479**, 1 (2002).

[22] H. Czyż and J. H. Kühn, Eur. Phys. J. C **18**, 497 (2001).

[23] R. R. Aekhmetshin *et al.* (CMD-2 Collaboration), Phys. Lett. B **466**, 392 (1999).

[24] A. Bondar *et al.*, Phys. Lett. B **466**, 403 (1999).

[25] A. B. Arbuzov *et al.*, J. High Energy Phys. 10 (1997) 001.

[26] M. Caffo, H. Czyż, and E. Remiddi, Nuovo Cimento Soc. Ital. Fis. A **110**, 515 (1997); Phys. Lett. B **327**, 369 (1994).

[27] E. Barberio, B. van Eijk, and Z. Was, Comput. Phys. Commun. **66**, 115 (1991).

[28] S. Agostinelli *et al.* (GEANT 4 Collaboration), Nucl. Instrum. Methods Phys. Res., Sect. A **506**, 250 (2003).

[29] T. Sjostrand, Comput. Phys. Commun. **82**, 74 (1994).

[30] S. Jadach and Z. Was, Comput. Phys. Commun. **85**, 453 (1995).

[31] K. Nakamura *et al.* (Particle Data Group), J. Phys. G **37**, 075021 (2010).

[32] F. Jegerlehner *et al.*, http://www-com.physik.hu-berlin.de/~fjeger/alphaQED.tar.gz.

[33] L. M. Kurdadze *et al.* (OLYA Collaboration), JETP Lett. **47**, 512 (1988) [http://www.jetpletters.ac.ru/ps/1096/article_16553.shtml].

[34] S. I. Dolinsky *et al.* (ND Collaboration), Phys. Rep. **202**, 99 (1991).

[35] M. N. Achasov *et al.* (SND Collaboration), J. Exp. Theor. Phys. **96**, 789 (2003).

[36] L. M. Barkov *et al.* (CMD Collaboration), Sov. J. Nucl. Phys. **47**, 248 (1988).

[37] R. R. Akhmetshin *et al.* (CMD-2 Collaboration), Phys. Lett. B **595**, 101 (2004).

[38] R. R. Akhmetshin *et al.* (CMD-2 Collaboration), Phys. Lett. B **491**, 81 (2000).

[39] R. R. Akhmetshin *et al.* (CMD-2 Collaboration), Phys. Lett. B **475**, 190 (2000).

[40] G. Cosme *et al.* (M3N Collaboration), Nucl. Phys. **B152**, 215 (1979).

[41] A. Cordier *et al.* (DM1 Collaboration), Phys. Lett. B **81**, 389 (1979); **109**, 129 (1982).

[42] D. Bisello *et al.* (DM2 Collaboration), Nucl. Phys. B, Proc. Suppl. **21**, 111 (1991).

[43] C. Bacci *et al.* (GG2 Collaboration), Phys. Lett. B **95**, 139 (1980).

[44] M. Davier, A. Hoecker, B. Malaescu, C. Z. Yuan, and Z. Zhang, Eur. Phys. J. C **66**, 1 (2010).

[45] H. Mendez *et al.* (CLEO Collaboration), Phys. Rev. D **78**, 011102R (2008).